Space Weather

RESEARCH ARTICLE
10.1029/2024SW003873

Influence of Solar Wind High-Speed Streams on the Brazilian Low-Latitude Ionosphere During the Descending Phase of Solar Cycle 24

S. P. Moraes-Santos[1], C. M. N. Cândido[2], F. Becker-Guedes[1], B. Nava[3], V. Klausner[2], C. Borries[4], F. S. Chingarandi[1], and T. O. Osanyin[1]

[1]National Institute for Space Research, São José dos Campos, Brazil, [2]University of the Vale of Paraíba, UNIVAP, São José dos Campos, Brazil, [3]The Abdus Salam International Centre for Theoretical Physics (ICTP), Trieste, Italy, [4]German Aerospace Center (DLR), Institute for Solar-Terrestrial Physics, Neustrelitz, Germany

Key Points:

- Statistical study on the low-latitude Vertical Total Electron Content in Brazilian longitudinal sector during the declining phase of SC 24 and Catalogs with the main results
- Low latitude daytime and nighttime ionospheric variations were observed up to 30 TECu and −20 TECu
- Effects of prompt penetration electric fields and disturbance dynamo electric fields in the Brazilian low latitude ionosphere: three case studies

Supporting Information:

Supporting Information may be found in the online version of this article.

Correspondence to:

S. P. Moraes-Santos,
stella.santos@inpe.br

Citation:

Moraes-Santos, S. P., Cândido, C. M. N., Becker-Guedes, F., Nava, B., Klausner, V., Borries, C., et al. (2024). Influence of Solar wind high-speed streams on the Brazilian low-latitude ionosphere during the descending phase of solar cycle 24. *Space Weather*, *22*, e2024SW003873. https://doi.org/10.1029/2024SW003873

Received 22 JAN 2024
Accepted 15 SEP 2024

Abstract This study investigates the Brazilian low-latitude ionospheric response to CIR/HSS-driven geomagnetic storms during the declining phase of solar cycle 24, from 2016 to 2017. In this period the geomagnetic storms were mostly moderate, $SymH_{min} \approx -72$ nT, $AE_{max} \approx 1580$ nT, $Vsw_{max} \approx 690$ km/s and lasted, on average, for 6 days. We analyze the variations in Vertical Total Electron Content (VTEC) at three representative regions: bele, over the equatorial region; boav and cuib, at the northern and southern crests of the Equatorial Ionization Anomaly. Our findings reveal the role of High-Speed Solar Wind Streams and Corotating Interaction Region—driven geomagnetic storms. The VTEC intensifications were up to 30 TECu, during the daytime and nighttime. Additionally, three categories of nighttime enhancements were observed and analyzed with distinct characteristics and levels of pre-reversal strengthening; Depletions up to 20 TECu also occurred during the day and nighttime. The delay between the storm commencement and the positive and negative variations were, on average, 7 and 20 hours, respectively. We discuss the Prompt Penetration Electric Fields and Disturbance Dynamo Electric Fields following the magnetic reconnection between Earth's and interplanetary magnetic field, using observational data and modeling. Furthermore, this study presents catalogs of low-latitude ionospheric storms, providing detailed information for space weather applications and ionospheric modeling.

Plain Language Summary This study examines the impact of solar wind on the low-latitude ionosphere, in Brazilian longitudinal sector, during the descending phase of the SC 24, 2016/2017. Specifically, we focused on High-Speed Solar wind Streams (HSS) and Corotating Interaction Regions (CIRs) that can cause disturbances in the Earth's magnetic field, leading to weak-to-moderate geomagnetic storms. Our findings show that these disturbances can affect the low-latitude ionosphere for several days. By analyzing the variations in the Vertical Total Electron Content (VTEC), we found that remarkable increases occur during the recovery phase of these storms, observed at the crests of the EIA. This study provides new insights into the effects of the solar wind on the Earth's atmosphere during moderate solar activity which can be of interest for space weather applications.

1. Introduction

The Total Electron Content (TEC) is one of the main parameters that allow a diagnosis of the ionosphere. It is a measure of the electrons along the line of sight from the satellite to the receiver, which is usually mapped to the vertical TEC (VTEC) by assuming that all free electrons are concentrating within a shell of infinitesimal thickness, that is, the single model layer (Natras et al., 2022). TEC exhibits diurnal variation (Kelley & Dao, 2009; Ogwala et al., 2019; Seemala & Valladares, 2011); a seasonal and semiannual behavior (Batista et al., 1994; B. G. Fejer et al., 2008; L. Liu et al., 2010), as well as a day-to-day variability associated with low-to-upper atmosphere coupling processes, for example, gravity waves activity (Abalde et al., 2009; Abdu, 2005; Otsuka et al., 2013). TEC can be drastically affected during magnetosphere-ionosphere-thermosphere (MIT) coupling under the disturbed geomagnetic conditions that may lead to disturbed electric fields. These electric fields that modulate the storm-time equatorial and low latitude ionosphere are prompt penetration electric fields (PPEF), which occur most strongly after large and sudden changes in high-latitude convection, and disturbance dynamo electric fields (DDEF), which in turn are generated by Joule heating and perturbations of global thermospheric circulation (Blanc & Richmond, 1980; B. G. Fejer et al., 1979, 2017; Richmond et al., 2003). The short-lived PPEF is highly correlated with the interplanetary magnetic field (IMF) Bz, within the solar wind. It also can be related to interplanetary forcings such as Coronal Mass Ejections (CMEs), also known as Interplanetary Coronal Mass

Ejections (ICMEs), and Corotating Interaction Regions (CIRs) also known as Stream Interaction Regions (SIRs) (Richardson, 2018; Richardson & Cane, 2010). In the dayside (nightside) ionosphere, a southward turning of Bz leads to an eastward (westward) electric field disturbance (B. G. Fejer, 2011; B. G. Fejer et al., 1979).

It is well known that high solar activity can severely affect the ionosphere (Balan et al., 2011; Farid et al., 2020; Hanson et al., 2019; Mannucci et al., 2005; Mishra et al., 2020; Valladares et al., 2009). However, unusually quiet and extended period of low solar activity from 2006 to 2010 has sparked renewed interest in the role of low solar activity (Emery et al., 2011; Gibson et al., 2009; Kavanagh & Denton, 2007; Verkhoglyadova et al., 2013). Between them there are transitional periods lasting for few years: the descending and ascending phase of solar cycle (SC). In the declining phase of the solar cycles (SCs), the most prominent solar structures are the coronal holes (CHs) which emanate High-Speed Solar wind Streams (HSS), a plasma which travels in the interplanetary space with speed higher than 400 km/s. The interaction between HSSs and precedent low-speed streams (LSS), is responsible by interaction regions which co-rotate with the sun, referred as corotation interaction region (CIRs). CIRs usually cause weak to moderate, long-duration (days), and recurrent geomagnetic storms (Matamba & Habarulema, 2018; Richardson, 2018; Tsurutani et al., 2006).

Some authors reported the high ionospheric variability during geomagnetic storms caused by CIRs/HSSs (Candido et al., 2018; S. Chakraborty et al., 2020; Kutiev et al., 2012; Lei et al., 2008; J. Liu et al., 2012; Matamba & Habarulema, 2018; Pedatella & Forbes, 2011; Verkhoglyadova et al., 2013; Yeeram, 2017), indicating a prominent level of variability of plasma densities and content. Verkhoglyadova et al. (2011) analyzed the global TEC variation during the Whole Heliospheric Interval (WHI) from March 2008 to April 2008 (solar minimum SC 23) and observed considerable TEC increases during CIR-HSS storms. They also have identified a distinct relationship between the infrared emission irradiated from the thermosphere and CIR-HSS intervals.

Some case studies of the ionospheric response to CIR/HSS-driven geomagnetic storms were also performed for different regions or periods (Azzouzi et al., 2016; Candido et al., 2018; M. Chakraborty et al., 2015; Migoya-Orue et al., 2016; Tulasi Ram et al., 2015). Candido et al. (2018) investigated the Brazilian equatorial and low-latitude ionospheric response during the WHI interval between March and April 2008. By analyzing VTEC, and other ionospheric parameters taken from Digisonde observations, they have observed that during HSS intervals, the VTEC increased by more than 130%, which can be comparable to intense storms. Studies also relate the ionospheric response to CIR/HSS in Brazil with periods of High-Intensity Long Duration Continuous Auroral Activity (HILDCAAs) (Koga et al., 2011; Negreti et al., 2017; Pereira Silva et al., 2017, 2020).

One important aspect of the VTEC response to the geomagnetic storms is the nighttime VTEC enhancement. Previous studies (Le et al., 2014; L. Liu et al., 2013; Wang et al., 2022; Yadav et al., 2020 and references therein) have reported ionospheric nighttime enhancement. Wang et al. (2022) has performed a statistical study on the equatorial ionospheric nighttime enhancement and has classified three types of these enhancements with respect to their morphology. Type 1 nighttime enhancement is characterized by a typical Equatorial Ionization Anomaly (EIA) structure, with two crests around 15°N and 15°S. However, instead of the crests dissipating after sunset, they persist throughout the night, gradually closing to the equator until 0 LT and disappearing afterward. Type 2 nighttime enhancement is characterized by the typical EIA structure, with two crests around 15°N and 15°S. Despite the EIA dissipating after sunset, there is an observed increase in TEC in the equatorial region, as if the plasma were contracting at the magnetic equator. Subsequently, this intensification also extends to both crests, appearing at higher latitudes but with weaker intensity. Type 3 nighttime enhancement is defined by a prominent single crest at a lower latitude (10°N in the example in Wang et al., 2022) until sunset. Following this, the TEC declines until a surge occurs, starting from 21 T, first noticeable in the "counter" region (the southern crest in this example). Subsequently, this increase spreads to the equatorial region and the other crest, albeit with less intensity, lasting until around 2 LT. In our results, we classify the nighttime enhancements according to Wang et al. (2022), applying the same criteria, $\Delta TEC \geq 2$ TECu for at least 1 hr, except the reference VTEC is the average of the 5 quietest days.

This paper is, to the best of our knowledge, the first attempt to characterize the ionospheric response during the whole descending phase of the SC 24, focusing on the TEC variation at equatorial region and at around the crests of EIA. Moreover, our findings enhance the understanding of space weather modeling and forecasts, particularly during moderate solar activity.

Table 1
The Stations, Their Locations, Latitude (°), Longitude (°), and Dip (°) Calculated With the International Geomagnetic Reference Field, IGRF-13 Model (Alken et al., 2021); Local Time, Dawn Time, Sunset Time, and Type of Instrument

Stations	Geo lat (°)	Geo long (°)	Dip (°)	LT	Dawn (LT)	Sunset (LT)	Instrument
boav Boa Vista -RR	2.8	−60.7	18.3	UT–4:00	6:15	18:15	GNSS
bele Belém- PR	−1.5	−48.5	−1.9	UT–3:12	6:15	18:30	GNSS/Magnetometer
salu São Luís–MA	−2.5	−44.3	−9.1	UT–2:54	5:55	17:59	Digisonde
piur Piura -Peru	−5.2	−80.6	12.4	UT–5:24	6:23	18:21	Magnetometer
jica Jicamarca Peru	−11.7	−76.7	0.4	UT–5:06	6:11	18:01	Magnetometer
cuib Cuiabá MS	−15.6	−56.1	−17.9	UT–3:42	6:25	18:25	GNSS
vass Vassouras RJ	−22.4	−43.7	−38.8	UT–2:54	6:09	17:40	Magnetometer

Note. All the stations are in Brazil, except for Jicamarca and Piura.

2. Data and Methodology

To characterize the solar and geomagnetic events associated with CIRs/HSSs, we analyzed a range of solar, interplanetary, and geomagnetic indices/parameters. These interplanetary parameters were measured by instruments onboard the ACE satellite and provided by the SPDF OMNIWeb database (https://omniweb.gsfc.nasa.gov/). They are the Solar wind speed, Vsw (km/s); the proton temperature, Tp (10^6 K); the proton density, Np (1/cm³); the dynamic pressure, P (nPa); the interplanetary magnetic field, IMF |B| and its components: Bx, By and Bz (nT); the interplanetary electric field Ey (mV/m) and the solar flux parameter/index, F10.7 (SFU), where 1 SFU = 10^{-22} W/Hz m^2 (Tapping, 2013). The coordinate system used is Geocentric Solar Magnetospheric (GSM) (Laundal & Richmond, 2017; Nakagawa et al., 2019). Additionally, we utilized geomagnetic data provided by OMNI Web, which includes the symmetric H geomagnetic field component (SymH) in nT, the 3-hr planetary *K* from Potsdam, and the auroral electrojet index (AE) in nT. The data is provided in universal time (UT). We classified the geomagnetic storms based on the criteria by Gonzalez et al. (1994) (−30 nT ≥ Dst > −50 nT for weak; −50 nT ≥ Dst > −100 nT for moderate and Dst ≤ −100 nT for intense storms), applied to SymH, a proxy for Dst.

To study the ionospheric response, we analyzed the VTEC parameter across three representative regions in Brazil: the north and south crests of the Equatorial Ionization Anomaly (EIA) at Boa Vista and Cuiabá (boav and cuib), with local times LT = UT–4 and LT = UT–3.7; and the equatorial region in Belém (bele) with LT = UT–3.2. The LTs were obtained as in Zhou et al. (2018). The coordinates and locations are detailed in Table 1 and Figure 1. The receiver independent exchange (RINEX) data was provided by the GNSS receivers network from RBMC (Rede Brasileira de Monitoramento Contínuo) managed by IBGE (Instituto Brasileiro de Geografia e Estatística) in Brazil (https://www.ibge.gov.br/en/geosciences/geodetic-positioning/geodetic-networks/20079-brazilian-network-for-continuous-monitoring-gnss-systems.html?lang=en-GB). The VTEC was calculated using the GPS Gopi version 3.03 analysis code developed at Boston College by Seemala and Valladares (2011) (https://seemala.blogspot.com/, accessed on 14 April 2022). This code uses pseudo-range and code phase observations at L1 and L2 frequency bands to reduce errors such as tropospheric delay and clock offsets. The elevation angles considered are above 30° (Seemala, 2012; Valladares et al., 2009 for more details).

The difference between the absolute VTEC and relative VTEC was calculated as follows:

$$\Delta\text{VTEC} = \text{VTEC} - \text{RTEC} \quad (1)$$

VTEC represents the absolute VTEC (ATEC), while RTEC (Relative VTEC) is the average VTEC value for each minute during the five quietest days (5QD) of the month. These 5QD are selected based on the Kp index and

10.1029/2024SW003873

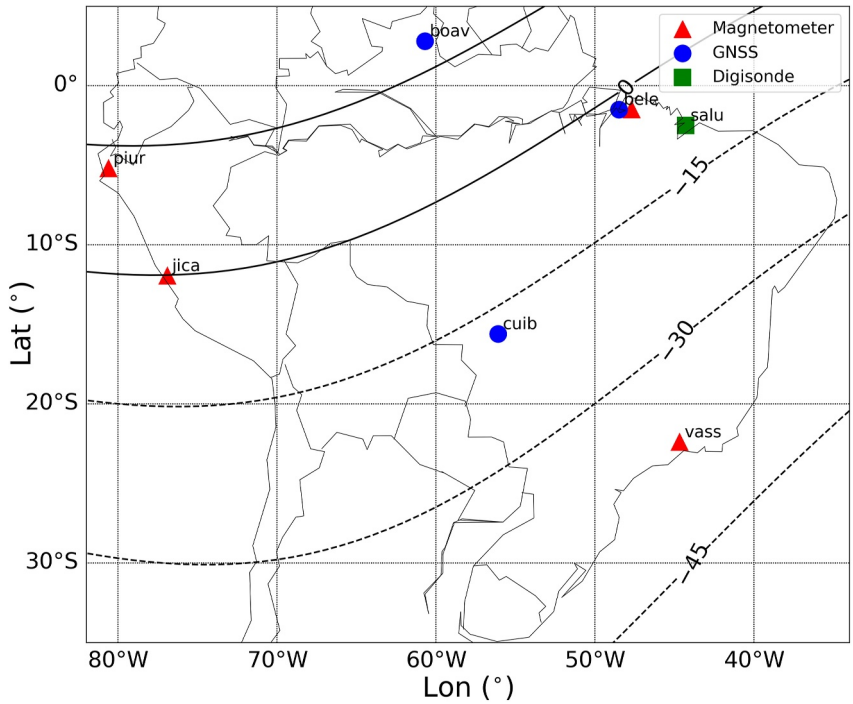

Figure 1. The map of South America showing the locations of GNSS, Digisonde, and magnetometer stations, along with latitude, longitude, and magnetic lines across the region. GNSS stations at the northern crest (boav, Dip: +18.3°) and southern crest (cuib, Dip: −17.9°), as well as the dip equator (bele, Dip: −1.9°), are indicated. The Digisonde station near the equator (salu, Dip: −9.1°) is also marked. Magnetometers used for drift calculations include one at the dip equator (bele, Dip: −1.9°; jica, Dip: +0.4°) and others outside the dip equator region (vass, Dip: −38.8°; piur, Dip: +12.4°). Red triangles denote magnetometers, a green square represents the Digisonde station near the dip equator, and blue circles indicate GNSS stations.

provided by the Kyoto World Data Center (WDC Kyoto, https://wdc.kugi.kyoto-u.ac.jp/qddays). RTEC for each minute is calculated by averaging the VTEC values corresponding to that minute across the five quietest days within the same month. This ensures that RTEC values accurately represent ionospheric conditions during periods of minimal activity. In months where not all 5QD are available, the available days are used instead. However, this situation only occurred in January 2016 for cuib and bele (day 30 is missing for bele and day 25 for cuib), and in May 2016 and December 2016 for boav (only day 4 is available in May, and day 30 is missing in December). The information concerning the number of quiet days available for all the stations is in the Tables S1 and S2.

The VTEC percentage deviation (δVTEC) was calculated as follows as reported by Candido et al. (2018) and references therein:

$$\delta\text{VTEC} = \left(\frac{\text{ATEC} - \text{RTEC}}{\text{RTEC}}\right) \times 100. \quad (2)$$

A statistical analysis and discussion on the features of the ionospheric response to moderate and few intense (SymH ≤ -50 nT) CIR/HSSs-driven geomagnetic storms, whose influence on the low latitude Brazilian ionosphere is investigated. Neither weak storms nor CME-driven storms or storms caused by other interplanetary structures were accounted for the study. We analyzed quantitative terms of δVTEC, including the timing and magnitude of its peak intensifications and decreases across distinct phases of geomagnetic storms. We identify geomagnetic storms triggered by CIRs/HSS by using interplanetary parameters, as follows: (a) We consulted the CHs report on Solen. Info (https://solen.info/solar/coronal_holes.html) and solar disk images at the same site for identifying CHs, (b). Then, we checked OmniWeb interplanetary and geomagnetic data set for the respective geomagnetic storms caused by them; (c) We identified a peak in Np followed by another in |B| prior to the geomagnetic storm, near the stream interface, (d) We use a threshold in solar wind velocity >400 km/s. These criteria were based on Tsurutani et al. (2006) and Grandin et al. (2015). The criteria were useful to differentiate the geomagnetic storms we aim to study from the ones caused by other solar forcings, like, for example, ICMEs. The

phases of the geomagnetic storms follow the classification by Gonzalez et al. (1994): initial phase, main phase (when SymH reaches its minimum, $SymH_{min}$), and recovery phase (returning to pre-storm conditions). We define the start of the main phase as when SymH first becomes negative and progresses toward reaching $SymH_{min}$. This point (t0) is chosen for studying ionospheric delay because not all geomagnetic storms caused by CIRs/HSSs exhibit sudden storm commencement (SSC) in SymH, as noted by Tsurutani et al. (2006). The main phase concludes when SymH reaches $SymH_{min}$. The recovery phase starts, entailing ongoing disturbances but with SymH returning to near-background values, close to 0 nT, indicating the end of the storm. All the information regarding the statistics of the geomagnetic storms is included in the Tables S3–S10.

We also present three case studies that are included in the statistics to highlight the characteristics of the geomagnetic storms and their effects. The first case occurred between 7 and 12 May, 2016. The second case occurred between 26 March and 3 April 2017. The third case occurred between 6 and 14 November, 2017. In these case studies, we analyzed interplanetary parameters (Vsw, Bz, and Ey), geomagnetic indexes (SymH and AE), the VTEC, RTEC, Digisonde data, drift data derived from magnetometers using the *H* component, and the solar flux (F10.7). For the case studies, daytime drift was calculated using the horizontal component (*H*) data from magnetometers available on the SAMBA-AMBER network, accessible at https://magnetometers.bc.edu/. The magnetometer stations chosen to calculate ΔH and obtain the drift were Belém (bele) and Vassouras (vass). We refer to Anderson et al. (2002), (2004); Yizengaw and Moldwin (2009), for obtaining the daytime drift. We selected one calm day, based on the quiet days from Kyoto, for each case, as the reference for the quiet time. This reference was repeated for each day of the storms. For the May 2016 case study, due to data unavailability from 7 May to 12 May on bele-vass, data from Jicamarca (jica) and Piura (piu) were used. The coordinates and locations can be found in Table 1 and Figure 1. Santos et al. (2016) already assumed that drifts over Jicamarca should be like the drifts over the equatorial sector in Brazil and justified that the zonal plasma drift and zonal wind velocities can be approximately equivalent. Furthermore, Digisonde observations from São Luis (salu) provided parameters such as F-region critical frequency (foF2), virtual height (h'F) in meters, and F-layer peak height (hmF2) in meters, processed using the SAO Explorer software package. The station coordinates are listed in Table 1 and Figure 1. For completeness, we employed the empirical vertical disturbance drift model developed by Fejer and Scherliess (1997b), Fejer and Scherliess (1997a) to examine the impact of DDEF and PPEF on the vertical **E** x **B** drift. This approach assesses the plasma drift perturbation by considering the combined effects of short-lived PPEF and longer-lasting DDEF in response to a time series with a 15-min resolution of AE indices. Additionally, it incorporates an analytical description of the quiet-time *F* region vertical drift from Scherliess and Fejer (1999), employing cubic-B splines and conservative electric fields. For more details, please refer to Fejer and Scherliess (1997b), Fejer and Scherliess (1997a) and Scherliess and Fejer (1999). Both models are in the International Reference Ionosphere model 2020 (Bilitza, 2018; Bilitza et al., 2022). In the of Supporting Information S1, we included plots of the interplanetary parameters and geomagnetic indices for the three geomagnetic storms, along with images of the coronal holes (CHs) that were the sources of these storms (Figures S1–S3 in Supporting Information S1). Additionally, we provided a compilation of GUVI O/N2 plots for the period, except for May 2016, which includes a previous mild storm (Figures S4–S6 in Supporting Information S1).

3. Results

Figure 2 shows the interplanetary and geomagnetic parameters and indices variation through the descending phase of the SC 24 from 2016 (left) to 2017 (right). From the top to bottom, the panels show: Vsw (km/s); P (nPa); Tp (10^6 K); Np (1/cm³); |B|, Bx, By, and Bz (nT); Ey (mV/m); SymH (nT); Kp; AE (nT) and the solar flux, F10.7 (SFU). The horizontal reference blue lines in the plots laying in the magnetic field |B|, its components Bx, By and Bz, Ey and SymH, indicates 0 nT. The horizontal dashed green lines over Vsw, SymH, Kp, and AE denote the lower boundary of moderate geomagnetic storms (Vsw = 400 km/s, SymH = −50 nT, Kp = 4, and AE = 1,000 nT). These reference lines make it easier to identify geomagnetic storms caused by CIRs, usually: $-50 \geq SymH < -100$ nT, $Kp > 4$, $AE > 1{,}000$ nT and $Vsw > 400$ km/s (Gonzalez et al., 1994; Kivelson et al., 1996; Loewe & Prölss, 1997; Tsurutani et al., 2006).

From 2016 to 2017, 23 moderate ($-50 \leq SymH \leq -100$ nT) and 3 intense ($SymH \leq -100$ nT) geomagnetic storms associated with CIR/HSSs structures were observed. All the information concerning these storms is gathered in catalog Table S3. The information concerning the delay, peak ΔVTEC and δVTEC for the three stations are gathered in catalogs Tables S4–S10.

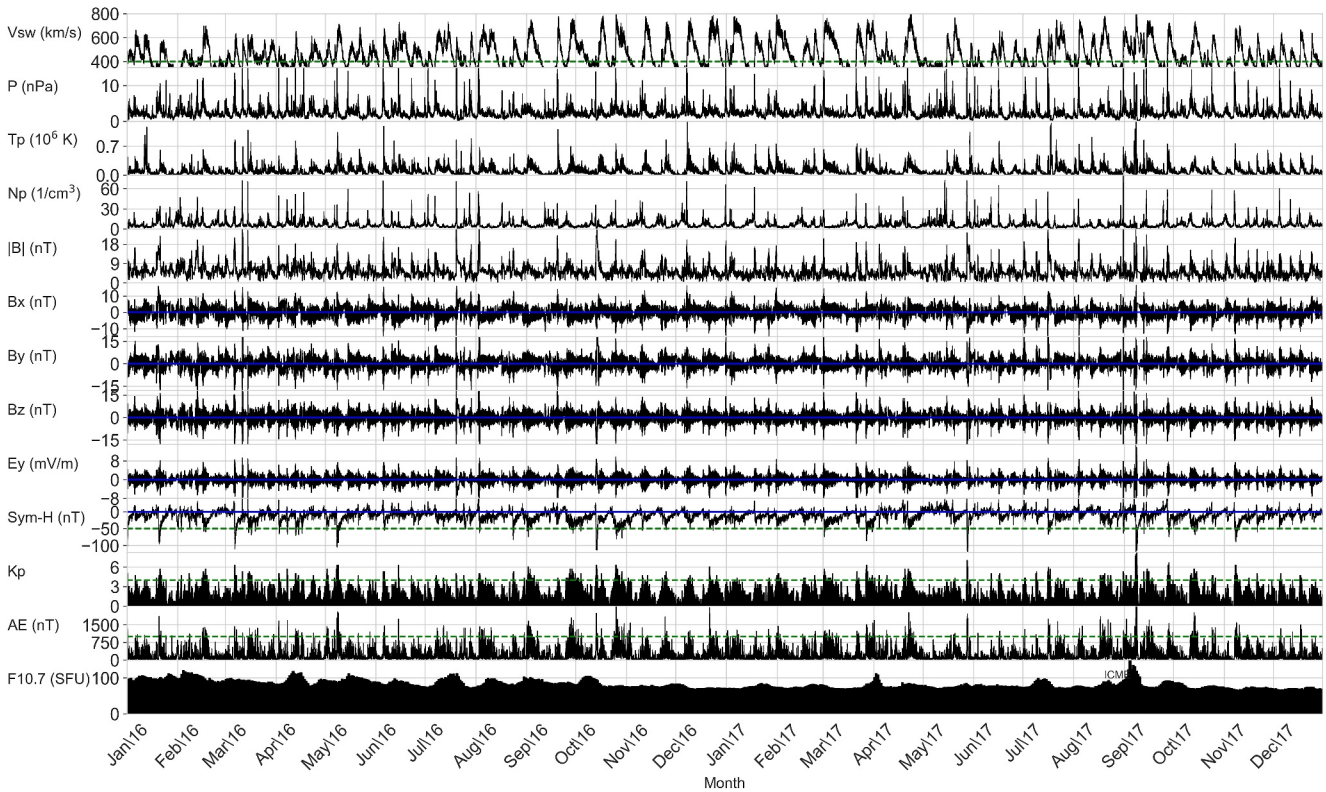

Figure 2. Solar, interplanetary parameters, and geomagnetic indices variation from 2016 to 2017. From top to bottom panels: Vsw (km/s); P (nPa); Tp (10^6 K); Np (1/cm³); IMF |B| and its components Bx, By and Bz (nT); Ey (mV/m); SymH (nT); Kp; AE (nT) and F10.7 (SFU). Dashed green lines represent, respectively: the solar wind speed = 400 km/s; the moderate storms SymH = −50 nT; the geomagnetic disturbance level, Kp = 4 and AE = 1,000 nT. The continuous blue lines represent the zero-reference line for IMF, IEF and SymH. In September 2017 there is an ICME event that is not included in our study, indicated in the last panel.

3.1. CIR/HSS Representative Case Studies

In this section, we present three case studies previously mentioned in Section 2. The first one took place in May 2016, during the southern winter solstice. The second case occurred in March 2017, in southern autumn equinox. Finally, the third case occurred in November 2017, in summer solstice. For detailed dates, please refer to Section 2–Data and Methodology. Figures showing the CHs, interplanetary parameters, and geomagnetic indexes, and thermospheric O/N2 are included in the Figures S1–S6 in Supporting Information S1.

3.1.1. Case Study 1–May 2016

Figure 3 shows an intense geomagnetic storm observed from 7 May to 12 May 2016. Panels (a to e) display Vsw (km/s), SymH (nT), IMF Bz (nT), Ey (mV/m), and AE (nT) respectively. Panel (f) shows the modeled disturbed (black line) and quiet time (gray) vertical E x B drift (m/s) at bele (dip: −1.9°; Lon = −48.5; LT = UT–3:18), equatorial region (Fejer & Scherliess, 1997a, 1997b; Scherliess & Fejer, 1999). Panel (g) depicts the daytime vertical drift (in black) and the quiet day on 25 May (in gray), calculated from magnetometer ΔH data from jica (dip: +0.4°; LT = UT–5:06) and piur (dip: +12.4°; LT = UT–5:24), due to the absence of magnetometer data in vass and bele during May 2016, as mentioned in Section 2. We refer to Yizengaw & Moldwin, 2009 for calculating the drifts. Panels (h and i) display the DDEF drift (m/s) and the PPEF drift (m/s), both obtained using the same model mentioned previously for panel (f). Panels (j and l) show the ionospheric parameters from Digisonde observations at salu (dip: −9.1°, LT = −2:54). They are the F-region critical frequency (foF2), the virtual height (h'F) in meters (m), and the F-layer peak height (hmF2) in meters (m). Panels (m, n, and o) display absolute VTEC (black) and relative VTEC (gray line) for boav (dip: +18.3°; LT = UT–4:00), bele (dip: −1.9°; LT = UT–3:18), and cuib (dip: −17.9°; LT = UT–3:42). The calculation of relative VTEC (RTEC), based on Equation 1 (ΔVTEC = VTEC—RTEC), involves averaging VTEC values during the five quietest days (5QD) of

10.1029/2024SW003873

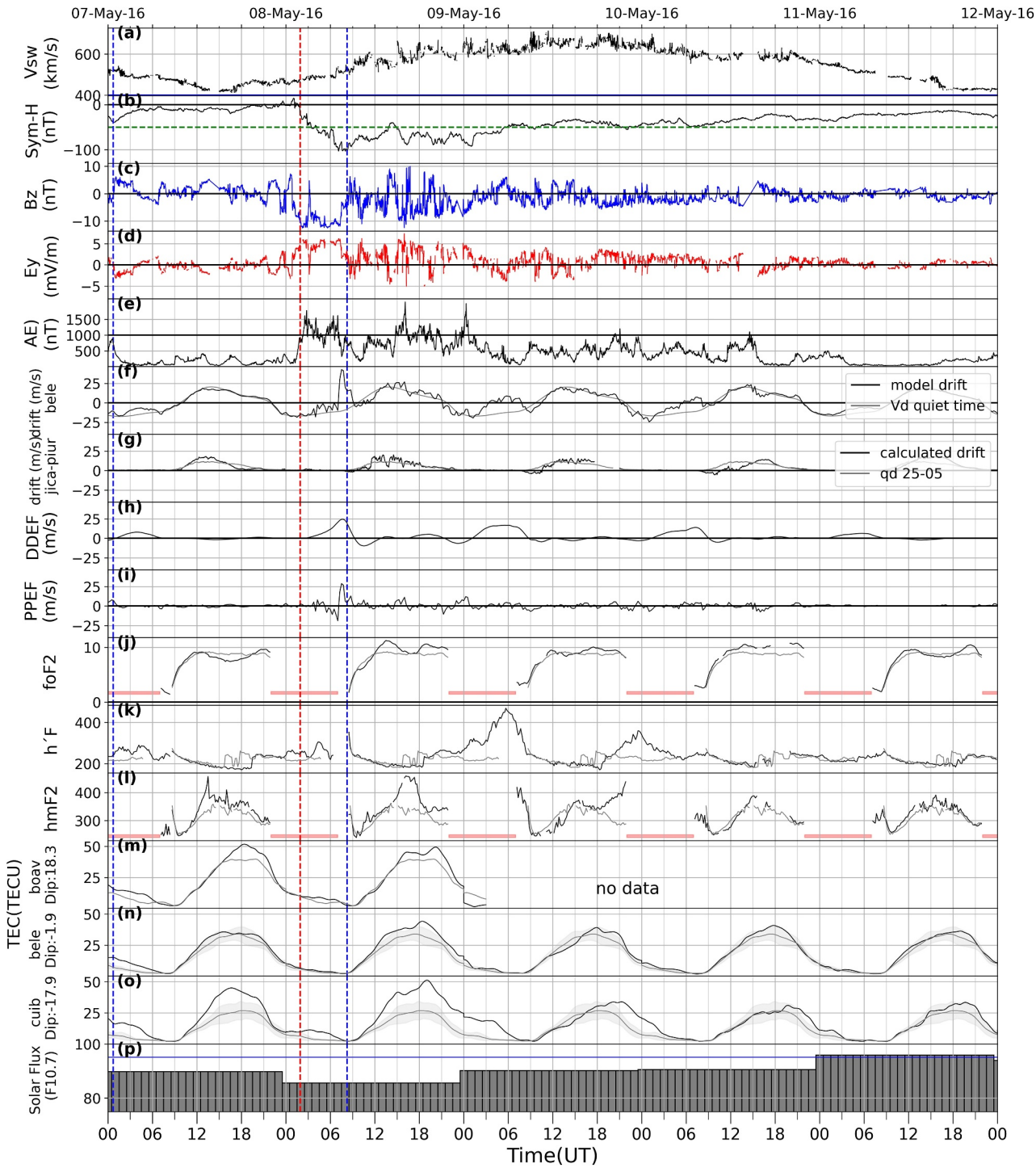

Figure 3. Interplanetary parameters, geomagnetic indexes, ionospheric parameters, and solar flux variations from 07 to 12 May 2016. The panels display: (a) Vsw (km/s), (b) SymH (nT), (c) Bz (nT), (d) Ey (mV/m), and (e) AE (nT). Panel (f) shows the modeled drift during the disturbed period (black line) and the quiet time (gray line), for bele. Panel (g) shows the calculated drift from jica-piur (black line) and the drift of the quiet day, 25 May (gray line). Additionally, panels (h, i) display the model DDEF and PPEF drifts (m/s, black lines). Panel (j) shows the critical frequency of the ionospheric F2 layer (foF2) in Hertz (black line) and the 3 quiet days average (3QD, gray line). Panel (k) depicts the minimum virtual height of trace F (h'F) in meters (black line) and the 3QD (gray line). Panel (l) illustrates the height of the peak electron density (hmF2) in meters (black line) and the 3QD (gray line) at salu (dip: −9.4°). From (m to o), the VTEC values (black line) and RTEC (gray line) for representative regions are shown, with the standard deviation depicted as shaded light gray. Panel (p) shows the flux F10.7 (gray bars) and the 5QD average of F10.7 (blue line). The blue continuous line in (a) indicates Vsw = 400 km/s. The continuous green dashed horizontal line in (b) is SymH = −50 nT. The vertical dashed red line indicates t0, and the blue one indicates $SymH_{min}$. The horizontal red bar in foF2 and hmF2 indicates the occurrence of Spread-F.

the month. The light gray shaded area represents the standard deviation range of RTEC. There are gaps of data in boav from 9 May that 0 UT (8 May at 20 UT, boav) to the rest of the storm. Panel (p) depicts the solar flux index, F10.7, with the average F10.7 (blue line) for the five quietest days of the month. The vertical dashed red line indicates t0, and the blue one indicates $SymH_{min}$. The horizontal red bar in foF2 and hmF2 indicates the occurrence of Spread-F. For more details about Spread-Fs, we refer to Abdu, 2001; Abdu et al., 1983; Burke et al., 2004; McClure et al., 1977; Rastogi, 1980 and references therein. The five quietest days of May 2016, as indicated by WDC Kyoto, were: 25, 26, 12, 23, and 4. At boav, it was only possible to use 4 May as the reference day, since there is a data gap from the 10 May to 26 May.

The dashed vertical red and blue lines represent, respectively, the t0 and the $SymH_{min}$. The highlight the star and the end of the main phase of the storm The top *x*-axis shows the days in UT. Days are shown at 0 UT. The bottom *x*-axis shows the hours in UT.

The intense geomagnetic storm interval begins at the onset of 8 May. During this interval, VTEC rises compared to the reference. It starts at 0 UT (21 LT) and reaches about 7 TECu at 3:30 UT (0:30 LT) in the EIA crests at night. This increase is observed 30 min after a southward turning of Bz, from 23:30 UT (20:30 LT) to 0:30 UT (21:30 LT).

The main phase starts on 8 May at 1:56 UT (21:56 LT, boav; 22:44 LT, bele; 22:14 LT, cuib) and $SymH_{min} = -105$ nT on 8 May at 8:15 UT (4:15 LT, boav; 05:03 LT, bele; 04:33 LT, cuib). During the main phase, the lowest value of Bz was −12.6 nT observed at 2 UT (22:00 LT, boav; 22:48 LT, bele; 22:18 LT, cuib). The Bz is steadily southward for 3 hr, with a small northward turn around 3 UT (23:00 LT, boav; 23:48 LT, bele; 23:18 LT, cuib). It becomes southward again until the end of the main phase at 8:15 UT (04:15 LT, boav; 05:03 LT, bele; 04:33 LT, cuib) of the same day. The AE index remains above 1,000 nT for approximately 6 hr.

During the initial phase of the intense geomagnetic storm, from the 23 UT (19:00 LT, boav; 19:48 LT, bele; 19:18 LT, cuib) of 7 May, a nighttime VTEC increase compared to RVTEC, in all stations started at 0 UT (20:00 LT, boav; 20:48 LT, bele; 20:18 LT, cuib). In boav, ΔVTEC–4 TEC on 8 May at 4 UT (7 May, 0 LT, boav); in bele VTEC ∼ RTEC; and cuib ΔVTEC–7 TECu on 8 May at 3 UT (7 May, 23:18 LT, cuib). These intensifications occurred 30 min after a southward turning of Bz, from 23:30 UT (19:30 LT, boav; 20:18 LT, bele; 19:48 LT, cuib) to 0:30 UT (20:30 LT, boav; 21:18 LT, bele; 20:48 LT, cuib). On 8 May at 9 UT (5:00 LT, boav; 5:48 LT, bele; 5:18 LT cuib), the Bz turns northward, and VTEC values are very similar to the RTEC all stations from 9 UT (5:00 LT, boav; 5:48 LT, bele; 5:18 LT cuib) to 11 UT (7:00 LT, boav; 7:48 LT, bele; 7:18 LT cuib). After this period, the VTEC values gradually intensified at cuib and bele, while in boav, the intensification started after 13 UT (9:00 LT, boav). The intensifications reach 11 TECu in boav at 20 UT (16:00 LT, boav), 12 TECu in bele at 18:40 UT (15:28 LT, bele), and in cuib 25 TECu at 19 UT (15:18 LT, cuib). These intensifications persisted through the night and into the first day of the recovery phase until at least 0 UT (20 LT, boav) in boav. After 9 May at 0 UT (20:00 LT, boav; 20:48 LT, bele; 20:18 LT, cuib), the intensification ceases in bele at 1 UT (21:18 LT) and keep with noteworthy VTEC enhancements of ∼18 TECu at the southern crest of the EIA, ceasing at 7 UT (3:18 LT, cuib). Concurrently, it is observed a DDEF ∼20 m/s in the model. The DDEF nighttime is eastward, and drives the *F* region uplift. Navarro et al., 2019 discuss that the reversal of the drift shifts to later local times with low solar flux and is the smallest in May, which seems to agree with our results. During the whole geomagnetic storm we observed intensifications in the rate of O/N2 in the low latitudes, compared to the quiet day as shown Figure S4 in Supporting Information S1. 4 May was chosen as the reference due to the unavailability of the other quiet days (25, 26, 23) and 12 May is the recovery phase of the storm.

3.1.2. Case Study 2 – March 2017

Figure 4 shows a moderate geomagnetic storm observed from 26 March to 3 April 2017. Panels (a to e) display Vsw (km/s), SymH (nT), IMF Bz (nT), Ey (mV/m), and AE (nT) respectively. Panel (f) shows the modeled disturbed (black line) and quiet time (gray) vertical E x B drift (m/s) at bele (dip: −1.9°; Lon = −48.5; LT = UT–3:18), equatorial region. Panel (g) depicts the daytime vertical drift (in black) and the quiet day 13 March (in gray), calculated from magnetometer ΔH data from bele (dip: −1.9°; LT = UT–3:12) and vass (dip: −38.8°; LT = UT–2:54). Panels (h and i) display the DDEF drift (m/s) and the PPEF drift (m/s). No Digisonde data close to the dip equator in Brazil was available in this period. Panels (j, k, and l) display VTEC (black) and RVTEC (gray line) for boav (dip: +18.3°; LT = UT–4:00), bele (dip: −1.9°; LT = UT–3:18), and cuib (dip: −17.9°;

10.1029/2024SW003873

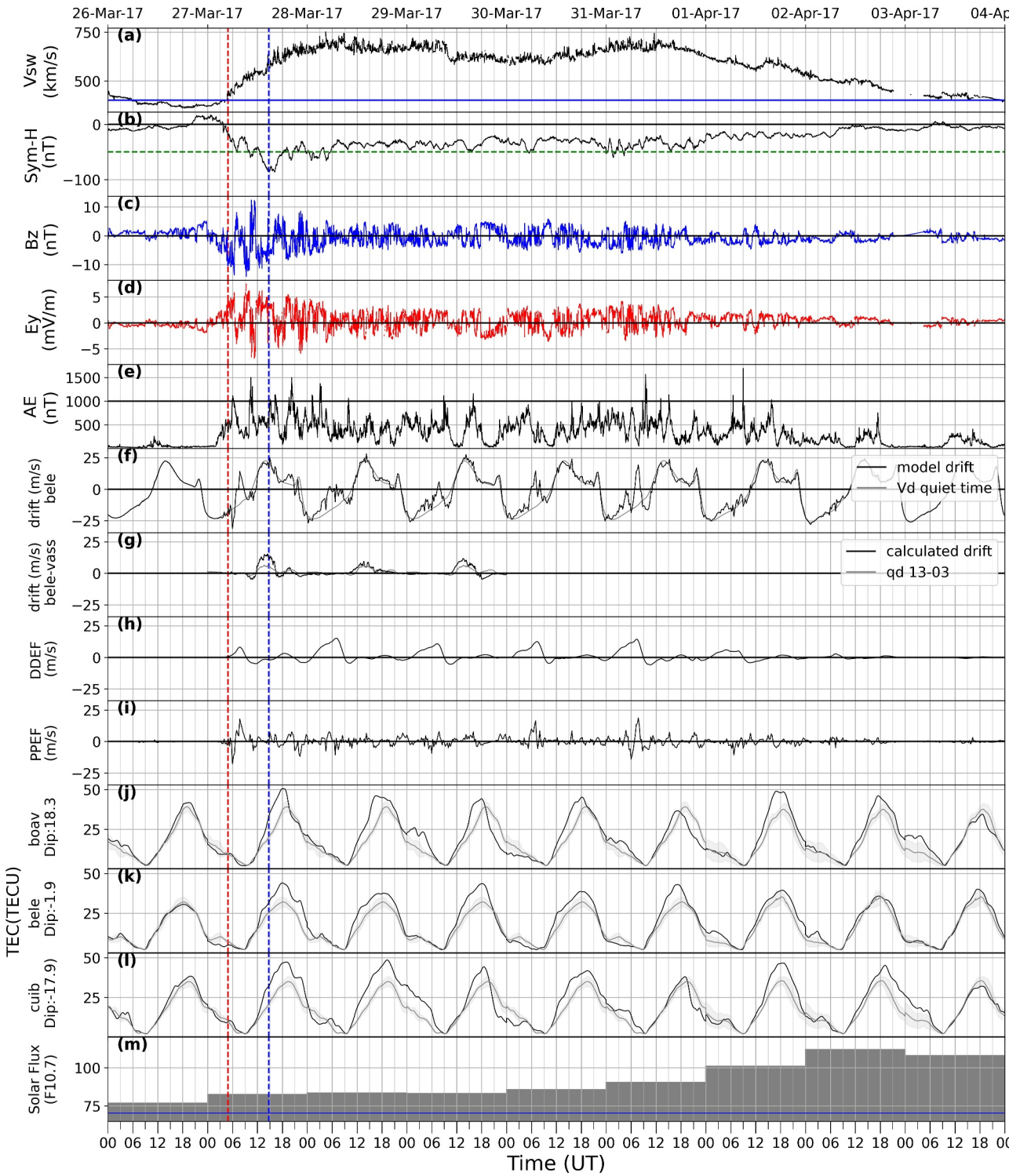

Figure 4. Interplanetary parameters, geomagnetic indexes, ionospheric parameters, and solar flux variations from 26 March to 4 April 2017. The panels display: (a) Vsw (km/s), (b) SymH (nT), (c) Bz (nT), (d) Ey (mV/m), and (e) AE (nT). Panel (f) shows the modeled drift during the disturbed period (black line) and the quiet time (gray line), for bele. Panel (g) shows the calculated drift from bele-vass (black line) and the drift of the quiet day, 13 March (gray line). Additionally, panels (h, i) display the model DDEF and PPEF drifts (m/s, black lines). From (j to l), the VTEC values (black line) and RTEC (gray line) for representative regions are shown, with the standard deviation depicted as shaded light gray. Panel (m) shows the flux F10.7 (gray bars) and the 5QD average of F10.7 (blue line). The vertical dashed red line indicates t0, and the blue one indicates $SymH_{min}$. The blue continuous line in (a) indicates Vsw = 400 km/s. The continuous green dashed horizontal line in (b) is SymH = −50 nT.

LT = UT–3:42). The light gray shaded area represents the standard deviation range of RTEC. Panel (m) depicts the solar flux index, F10.7, with the average F10.7 (blue line) for the five quietest days of the month. The five quietest days of March 2017, as indicated by WDC Kyoto were: 20, 19, 18, 13 and 17.

The start of the geomagnetic storm's main phase occurred on 27 March at 4:55 UT (0:55 LT, boav; 1:43 LT, bele; 1:13 LT cuib) (t0). Currently, the solar wind speed (Vsw) has increased from 395 to 650 km/s, in 12 hr and the values have been >400 km/s over 6 days. The velocity reached a maximum Vsw_{max} = 751.6 km/s on 28 March at 04:26 UT. The geomagnetic storm associated with the event is considered moderate according to Gonzalez et al. (1994), $SymH_{min}$ = −86 nT on 27 March at 16:15 UT (12:15 LT, boav; 13:03 LT, bele; 12:33 LT cuib). During the main phase of the storm, auroral activity (AE) intensifications were observed starting from 27 March at 3 UT. Peak intensities occurred at 1,374 nT on 27 March at 10:30 UT. In the recovery phase, AE peaked at 1,505 nT on 28 March at 3 UT, 1,568 nT on 31 March at 9:30 UT, and 1,696 nT on 1 April at 9 UT, indicating heightened geomagnetic activity throughout the storm period. The magnetic field component Bz exhibits oscillations during the main phase of the storm. The minimum value of Bz (Bz_{min}) reaches −14.1 nT. However, this southward orientation is sustained for less than 2 hr during the beginning of the main phase. In the end of the main phase, Bz is negative from 11 UT (7:00 LT, boav; 7:48 LT, bele; 7:18 LT cuib) to 16 UT (7:00 LT, boav; 7:48 LT, bele; 7:18 LT cuib) to. During the recovery phase, which spans 6 days, the Bz component continues to exhibit prominent levels of oscillation, fluctuating between southward and northward orientations multiple times. Our results show VTEC in all stations was close to the reference line in the beginning of the main phase since it was in the nighttime sector. VTEC intensifications occurs after 27 March at 12 UT (08:00 LT, boav; 08:48 LT, bele; 08:18 LT, cuib) in all stations. The maximum ΔVTEC for this day ($\Delta VTEC_{maxday}$) occurred: in boav, $\Delta VTEC_{maxday}$ = 16 TECu at 16 UT (12:00 LT, boav); in bele, $\Delta VTEC_{maxday}$ = 15 TECu at 22:32 UT (19:20 LT, bele) and in cuib, $\Delta VTEC_{maxday}$ = 15.4 TECu at 22:40 UT (18:58 LT, cuib). During daytime, there were observed increases in the drift velocity of the magnetometer, despite the drift model closely matching the reference quiet time. This difference could be attributed to the utilization of the AE index as an input to the model. It is worth noting that the AE index exclusively demonstrates nighttime peaks during this period. In boav, the intensifications last until after the main phase at 18 UT (14:00 LT, boav), while in cuib the intensification goes on until 28 March at 0 UT (27 March, 20:18 LT, cuib) and at bele it will end on 28 March at 2 UT (27 March, 22:48 LT, bele). Nighttime enhancements occur on every day, from 28 March to 3 April, except on 30 March, when from 21 UT (17:00 LT, boav; 17:48 LT, bele; 17:18 LT, cuib) until 5 UT (01:00 LT, boav; 01:48 LT, bele; 01:18 LT, cuib), VTEC decreases are observed compared to the RTEC. It is noteworthy that these effects occur when the Bz component of the IMF is more positive than negative for approximately 6 hr. However, the Bz magnitude is only around 5 nT. This is correlated to the period of increased levels of geomagnetic activity on the main phase during daytime.

3.1.3. Case Study 3–November 2017

Figure 5 shows a moderate geomagnetic storm observed from 6 November to 14 November 2017. Panels (a to e) display Vsw (km/s), SymH (nT), IMF Bz (nT), Ey (mV/m), and AE (nT) respectively. Panel (f) shows the modeled disturbed (black line) and quiet time (gray) vertical E x B drift (m/s) at bele (dip: −1.9°; Lon = −48.5; LT = UT–3:18), equatorial region. Panel (g) depicts the daytime vertical drift (in black) and the quiet day on 6 November (in gray), calculated from bele-vass. Panels (h and i) display the DDEF drift (m/s) and the PPEF drift (m/s). Panels (j and l) show the ionospheric parameters from Digisonde observations at salu: the F-region critical frequency (foF2), the virtual height (h'F) in meters (m), and the F-layer peak height (hmF2) in meters (m). Panels (m, n, and o) display absolute VTEC (black) and relative VTEC (gray line) for boav, bele and cuib. The light gray shaded area represents the standard deviation range of RTEC. Panel (p) depicts the solar flux index, F10.7, with the average F10.7 (blue line) for the five quietest days of the month. The vertical dashed red line indicates t0, and the blue one indicates $SymH_{min}$. The horizontal red bar in foF2 and hmF2 indicates the occurrence of Spread-F. The quietest days of November 2017, per WDC Kyoto, were: 6, 5, 26, 1, and 4.

The main phase of the geomagnetic storm spanned from 7 November, 8:46 UT (boav; 05:34 LT, bele; 05:04 LT, cuib) to 8 November, 4:04 UT (00:04 LT, boav; 00:52 LT, bele; 00:22 LT, cuib) with $SymH_{min}$ reaching −89 nT. Notably, 6 November exhibits a period of "calm before the storm" with Vsw < 400 km/s, SymH, Bz, Ey ≈ 0 nT, AE–25 nT, and Kp < 1.5 for over 6 hr. We refer to Borovsky & Steinberg, 2006, for more details on "calm before the storm." Ionospheric parameters also reflect this calm state. During the main phase, AE peaked at 1,172 nT at 19:17 UT (15:17 LT, boav; 16:05 LT, bele; 15:35 LT, cuib), staying below 1,000 nT. Bz is initially southward

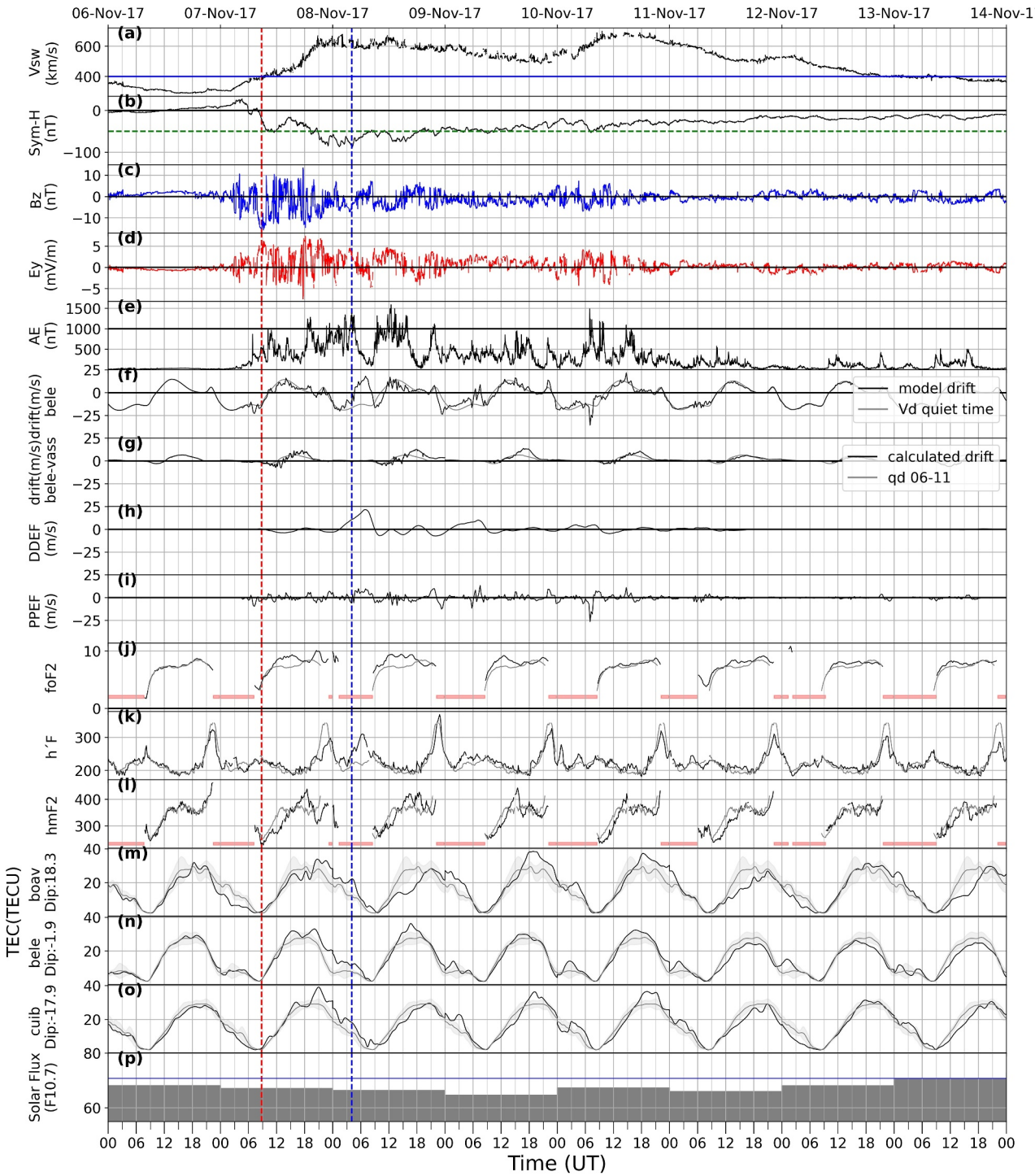

Figure 5. Interplanetary parameters, geomagnetic indexes, ionospheric parameters, and solar flux variations from 6 November to 12 November 2017. The panels display: (a) Vsw (km/s), (b) SymH (nT), (c) Bz (nT), (d) Ey (mV/m), and (e) AE (nT). Panel (f) shows the modeled drift during the disturbed period (black line) and the quiet time (gray line), for bele. Panel (g) shows the calculated drift form bele-vass (black line) and the drift of the quiet day, 6 November (gray line). Additionally, panels (h, i) display the model DDEF and PPEF drifts (m/s, black lines). Panel (j) shows the critical frequency of the ionospheric F2 layer (foF2) in Hertz (black line) and the 3 quiet days average (3QD, gray line). Panel (k) depicts the minimum virtual height of trace F (h'F) in meters (black line) and the 3QD (gray line). Panel (l) illustrates the height of the peak electron density (hmF2) in meters (black line) and the 3QD (gray line) at salu (dip: −9.4°). From (m to o), the VTEC values (black line) and RTEC (gray line) for representative regions are shown, with the standard deviation depicted as shaded light gray. Panel (p) shows the flux F10.7 (gray bars) and the 5QD average of F10.7 (blue line). The vertical dashed red line indicates t0, and the blue one indicates SymHmin. The blue continuous line in (a) indicates Vsw = 400 km/s. The continuous green dashed horizontal line in (b) is SymH = −50 nT. The horizontal red bar in foF2 and hmF2 indicates the occurrence of Spread-F.

from 9 UT (05:00 LT, boav; 05:48 LT, bele; 05:18 LT, cuib) to 12 UT (08:00 LT, boav; 08:48 LT, bele; 08:18 LT, cuib), then resumed from 12 UT (08:00 LT, boav; 08:48 LT, bele; 08:18 LT, cuib) to 15 UT (11:00 LT, boav; 11:48 LT, bele; 11:18 LT, cuib), persisting mostly southward thereafter. The recovery phase began promptly after, lasting from 7 November at 6:51 UT (02:51 LT, boav; 03:39 LT, bele; 03:09 LT, cuib) to 11 November at 15:15 UT (11:15 LT, boav; 12:03 LT, bele; 11:33 LT, cuib) on. The storm concluded on 13 November with solar wind velocity dropping below 400 km/s.

In the initial phase, on 7 November at 7 UT (03:00 LT, boav; 03:48 LT, bele; 03:18 LT, cuib), VTEC values closely RTEC in all stations. The model suggests that negative contributions from PPEF (∼-1.8 nT) correlate with a decrease in hmF2 relative to the baseline.

During the first hours of the main phase of the geomagnetic storm, from 7 November, from 9 UT (05:00 LT, boav; 05:48 LT, bele; 05:18 LT, cuib) to 18 UT (14:00 LT, boav; 14:48 LT, bele; 14:18 LT, cuib), the VTEC starts increasing to values exceeding RTEC in bele from 13 UT (09:00 LT, boav; 09:48 LT, bele; 09:18 LT, cuib; 10:06 LT, salu). Concurrently, foF2, h'F, and hmF2 were below the average in salu. In the northern crest of the EIA, boav, the VTEC was under RTEC, and at the southern crest of EIA, cuib, VTEC was close to the reference. After 18 UT, the AE index reached 1,000 nT, indicating a sudden increase in auroral activity. VTEC intensifications were observed in boav, bele, and cuib from 19 UT (15:00 LT, boav; 15:48 LT, bele; 15:18 LT, cuib) throughout the afternoon, night, and pre-dawn period.

In the recovery phase on 8 November, in all stations, VTEC exceeded RTEC by approximately 5 TECu at all stations around 5 UT (01:00 LT, boav; 01:48 LT, bele; 01:18 LT, cuib; 02:06 LT, salu). Concurrently, an increase in h'F was observed in Salu, although no data were available for hmF2 during this period.

On 13 November, the VTEC in bele exceeded RTEC from 0 UT (20:00 LT, boav; 20:48 LT, bele; 20:18 LT, cuib; 21:06 LT, salu) to 3 UT (23:00 LT, boav; 23:48 LT, bele; 23:18 LT, cuib; 00:06 LT, salu). Both h'F and foF2 presented values similar to the average. In boav and cuib VTEC values were below the reference. The cause of this decline remains unclear based on our available data, warranting further investigation as our data do not show any corresponding decreases.

3.2. Statistical Study of the Brazilian Low-Latitude VTEC During CIR/HSS-Driven Geomagnetic Storms in 2016–2017

In this section, we present the results of a statistical study on the Brazilian low-latitude ionospheric response to moderate geomagnetic storms caused by HSSs and CIRs from 2016 to 2017. In our study, we employed two statistical approaches. We have analyzed the maximum positive and negative variations in VTEC as a percentage deviation from the mean of the five quietest days. Additionally, we investigated the maximum positive and negative ΔVTEC compared to the mean of the five quietest days.

Figure 6 presents four histograms illustrating the main characteristics of the geomagnetic storms, including solar wind velocity (Vsw_{max}, km/s), the storm duration (Δ Storm, hours), the $SymH_{min}$ (nT), and maximum AE (AE_{max}, nT). Each histogram includes the occurrence of the measured values and the mean values indicated by a red dashed line. The histogram for Vsw_{max} shows values ranging from 400 to 800 km/s, with a mean of 684.2 km/s. Most occurrences are concentrated around 700 km/s, accounting for 42.3% of the total. The Δ Storm histogram displays values from 25 to 275 hr, with an average of 144.7 hr (144.7/24 – 6 days). Most occurrences are concentrated around 175 hr, accounting for 32% of the total. The $SymH_{min}$ histogram ranges from −120 to–60 nT, with a mean of −71.6 nT. Most occurrences are concentrated at −60 nT, accounting for 61.5% of the total. The AE_{max} histogram displays values from 700 to 2,500, with a mean of 1,576.5 nT. Most occurrences are concentrated around 1,450 nT, accounting for 38% of the total. These features seem to agree with the ones expected for HSS and CIRs events, according to the literature (Alves et al., 2006; Richardson, 2013, 2018; Richardson et al., 2006; Tsurutani et al., 2006).

Figure 7 displays six histograms representing the ionospheric storm delays (ΔT_d). The ionospheric storm delay refers to the time interval between the onset of geomagnetic storms and the onset of the ionospheric variations (ionospheric storms). Some studies have already discussed this feature (Balan & Rao, 1990; J. Liu et al., 2010; Zhang et al., 2021). The positive storm, PS, where VTEC > RTEC, are represented in gray and the negative storms, NS, where VTEC < RTEC, NS, in white. The red dashed lines represent the average, and the green dashed

10.1029/2024SW003873

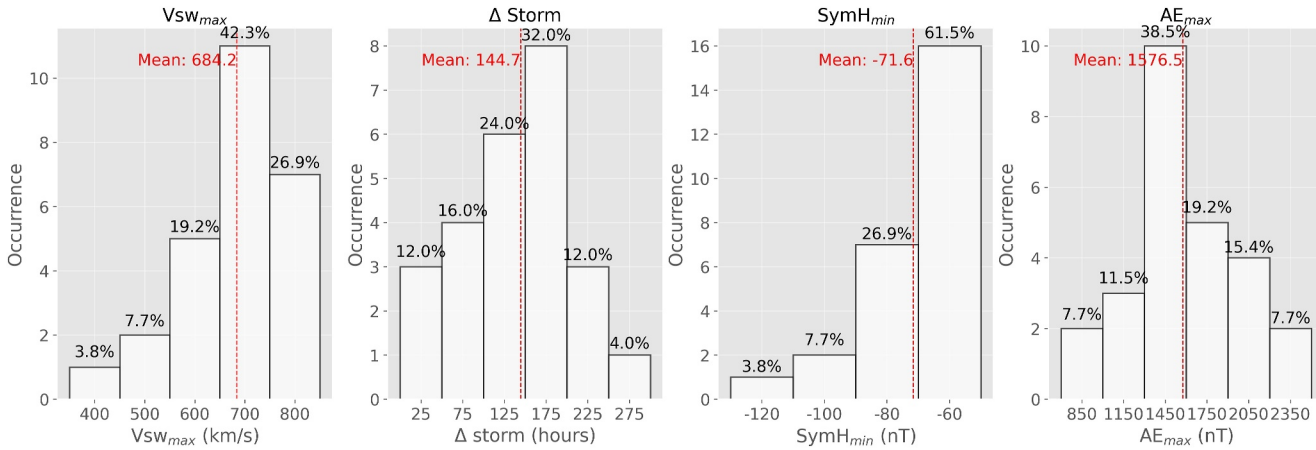

Figure 6. Histogram of maximum solar wind velocity in km/s (Vsw_{max}); the duration of the storm, in hours (ΔStorm); $SymH_{min}$, in nT and maximum AE, in nT (AE_{max}). The dashed red line represents the mean values.

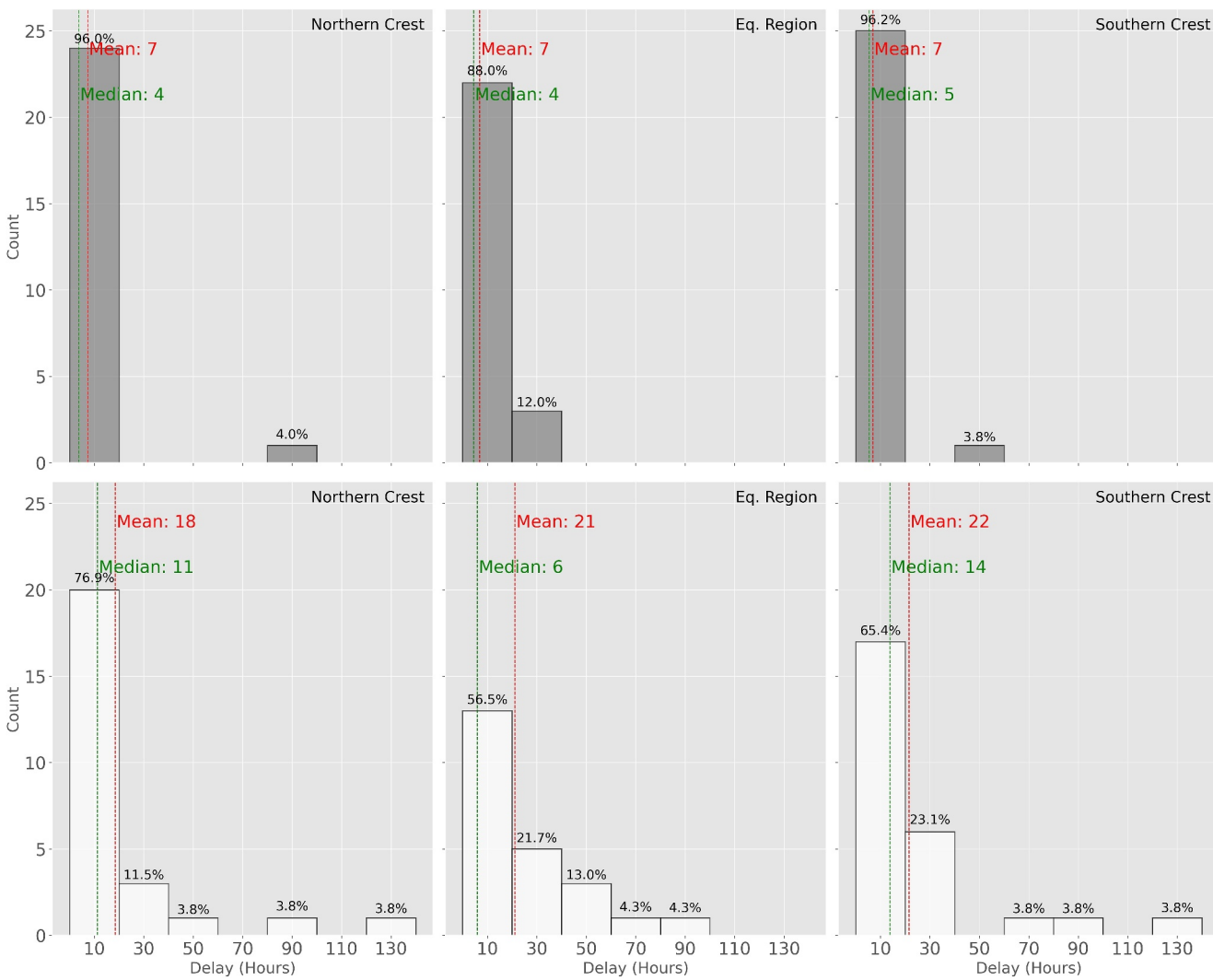

Figure 7. Histograms of ΔT_d. In gray, are the positive ionospheric storms. In white, negative ionospheric storms. The red dashed line represents the mean and the green ones the median.

10.1029/2024SW003873

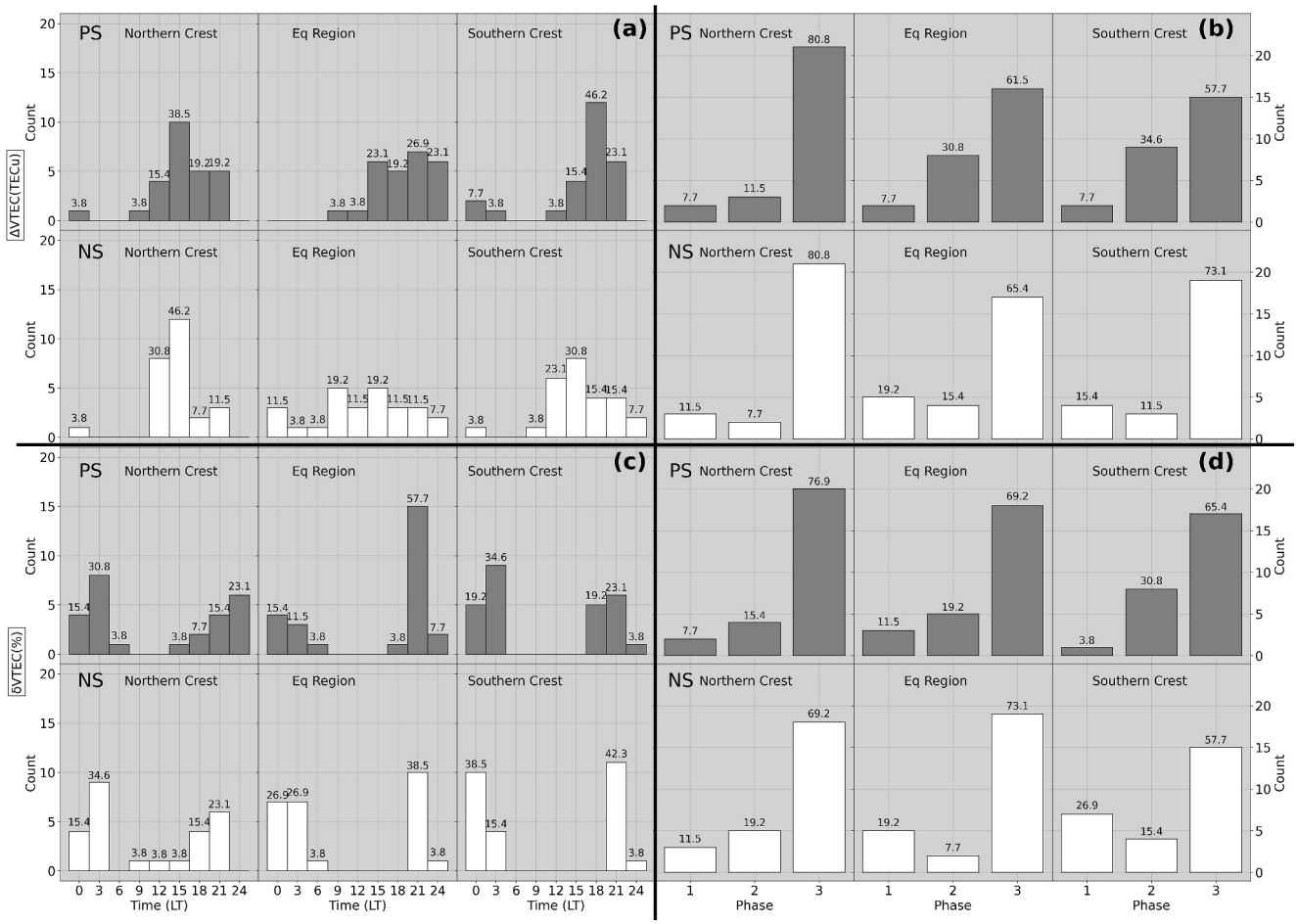

Figure 8. Statistics of VTEC response to HSS/CIRs geomagnetic storms. Panels (a, b) are, respectively, the analysis of ΔVTEC of each storm by local time and phase of the storm: 1–initial phase, 2–main phase and 3–recovery phase. Gray refers to positive ionospheric storm and white to negative ionospheric storm. Panels (c, d) are the statistics for δ VTEC.

lines represent the median. We considered the onset of positive or negative storm when the positive or negative δVTEC reaches 25% and then we calculated the time interval from the beginning of the geomagnetic storm. The histogram ranges from 10 to 130 hr. The bin size of the histograms is 20 hr. From the figure, one can observe that over boav, in 96% of the cases, the delay took 20 hr for the PS, and 76.9% of NS occurred within 20 hr. In bele, 88% of the delays for PS took 20 hr, and 56.5% of the occurrences for the NS took 20 hr. And in cuib, 96.2% and 65.4% of the occurrences took 20 hr for the PS and NS. The PS average delay took approximately 7 hr, while the NS average was around 18 hr (red dashed vertical lines). The PS usually takes less time to occur after t0 compared to the NS for all observed regions. This result is also available in S4 in the Supporting Information.

Figure 8 consists of four sets of six histograms labeled as (a), (b), (c), and (d). Each subplot displays the distribution of maximum and minimum ΔVTEC (a, b) and δVTEC (c, d) at three stations: boav (northern crest), bele (equatorial region), and cuib (southern crest). The figures depict the data relative to local time (LT) (a, c) and phases of the geomagnetic storm (b, d). Positive ionospheric storms (PS) $\Delta VTEC_{max}$ are shaded in gray, while negative ionospheric storms $\Delta VTEC_{min}$ (NS) are shown in white. In Figure 8a, during the PS, significant counts were observed at 15 LT (38.5%) in the northern crest (NC), at 21 LT (26.9%) in the equatorial region (Eq), and at 18 LT (46.2%) in the southern crest (SC). During the NS, for the NC, significant counts were noted at 15 LT (46.2%), distributed thought the day but primarily at 9 LT (19.2%) and at 15 LT (19.2%) in the Eq, and at 15 LT (30.8%) in the SC. Figure 8c shows $\delta VTEC_{max}$ during the PS (gray): significant counts occurred at 3 LT (30.8%) in the NC, at 21 LT (57.7%) in the Eq, and at 3 LT (34.6%) in the SC. During the NS (white), the $\delta VTEC_{min}$ in the NC exhibited most counts at 3 LT (34.6%), in the Eq at 21 LT (30.8%) and 15 LT (20.8%), and in the SC at 21 LT

(42.3%). These results indicate differences when analyzing the ΔVTEC and δVTEC variations both for PS and NS. When analyzing the ΔVTEC, the positive storms occur more during daytime, from 15 to 18 LT in the crests. Over the equatorial region, the intensifications occur more at nighttime before midnight. For the NS, the highest decreases in ΔVTEC occur during all day long, especially during daytime. When analyzing δVTEC, the maximum intensifications occur during the nighttime in all stations after the Pre-Reversal Enhancement (PRE). The δVTEC depletions occurs mostly during nighttime either, except in the NC, that occurred during the daytime too.

In panels (b and d), histograms depict the variations in ΔVTEC and δVTEC per storm phase, which are: 1–initial phase, 2–main phase and 3–recovery phase. Like panels (a and c), the gray rectangles represent positive storms, while the white rectangles represent negative storms. Notably, the most significant variations, whether measured in TECu or percentage, occur during the recovery phase at all stations, in both PS and NS.

It is worth mentioning that the catalogs we have created to gather information on CIR/HSSs-driven events provides a comprehensive summary of the main characteristics of the observed geomagnetic storms. It includes the interval, the duration and the onset and ending of main phase (t0 and $SymH_{min}$ date and time), the duration of the storm in hours, the Vsw_{max}, the average solar flux, the maximum solar flux, the Bz_{min}, AE_{max} and Kp_{max}. We also included a catalog for the delay, its date and time (in UT). Additionally, we also included the maximum and minimum ΔVTEC ($\Delta VTEC_{max}$ and $\Delta VTEC_{min}$) and maximum and minimum δVTEC ($\delta VTEC_{max}$ and $\delta VTEC_{min}$) for the boav, bele and salu. The catalogs are in the as Table S3 (interplanetary), Table S4 (T_d), Table S5 (ΔVTEC boav), Table S6 (ΔVTEC bele), Table S7 (ΔVTEC cuib), Table S8 (δVTEC boav), Table S9 (δVTEC bele) and Table S10 (δVTEC cuib).

4. Discussion

Intense and transient ICME-driven storms, in general, have been extensively studied, while CIR/HSS-driven storms have received more attention since the advent of recent deep solar minima. This investigation shows that CIR/HSS-driven storms are typically weak to moderate, long-duration disturbances and can affect the low-latitude ionosphere in several ways. Electric fields and auroral activity play a fundamental role on the low-latitude ionosphere, in the main phase, although it is observed that these effects are more pronounced during the recovery phase. In this work, we performed a statistical analysis of CIR/HSSs-driven storms and their influence on the low-latitude ionosphere in Brazil during the descending phase of SC 24. We analyzed VTEC in terms of ΔVTEC and δVTEC. This derived-TEC parameter provides additional insights into storm time ionospheric variations, since δVTEC is more sensitive to variations after local midnight, when VTEC values are significantly depleted (Immel & Mannucci, 2013). Our main findings are summarized as follows:

1. VTEC can be intensified (positive ionospheric storm) from the equator to low latitudes, over 100% compared to the RTEC as shown in the tables on Table S8 (δVTEC boav), Table S9 (δVTEC bele) and Table S10 (δVTEC cuib).
2. δVTEC (%) intensifications occur more frequently around 21:00 LT over the Equatorial region and around 03:00 LT at the crests of the EIA.
3. The highest observed δVTEC was ∼428% in cuib (south crest of EIA) in May 2016, ∼231% in bele (equatorial region) and ∼182% in boav (north crest of EIA), at nighttime.
4. ΔVTEC intensifications persist for several days during the recovery phase of storms, typically lasting around 144 hr (∼6 days).
5. ΔVTEC values exceeded 30 TECu at the crests of the EIA (shown in the Tables S5 and S7) and surpassed 20 TECu over the equatorial region (Table S6).
6. The daytime ΔVTEC can reach 26.5 TECu at the Northern crest of the EIA around 15:46 LT. Besides, over the equatorial region, ΔVTEC it is ∼23.6 TECu around 16:53 LT. Finally, in the Southern crest, it observed the highest ΔVTEC, at ∼ was 31.6 TECu around 19:13 LT (Tables S5–S7)
7. The nighttime intensifications were categorized in three types as pointed out in the Asian-Australian sector by Wang et al. (2022).

In the next sections we will discuss the most likely mechanism responsible for these daytime nighttime intensifications. We considered daytime from 6 LT to 17:59 LT and nighttime from 18 LT to 05:59 LT.

4.1. Daytime VTEC Variations

The statistical analysis and case studies present daytime variations in VTEC observed at three representative regions (boav, bele, and salu) during the main and recovery phases of the storms. Daytime variations are believed to be due to the combined effects of PPEF, solar ionization, auroral activity, neutral composition changes, and disturbed meridional neutral winds during storm time (H. Liu et al., 2021; Venkatesh et al., 2015). TEC depletions, shown by ΔVTEC, were observed predominantly during daytime, as shown in Figure 8a, which spans the range of daytime depletions from 9 LT to 18 LT.

The highest daytime intensifications were observed in the afternoon, at ∼ 15:00 LT, at the crests of the EIA, boav (northern crest), and cuib (southern crest), respectively, during the recovery phase of the storm, with $\Delta VTEC_{max} > 23$ TECu. On the other hand, over the equatorial region, bele, the highest daytime intensification occurred in the pre-sunset, ∼17:00 LT, with $\Delta VTEC_{max} = 24$ TECu.

The daytime intensifications occurring during the main phase of the storms are usually related to PPEF due to IMF Bz in the CIR (Verkhoglyadova et al., 2011), as presented in Figure 5 (Case 3). During the storm time, a southward turning of Bz initiates a substorm marked by AE activity intensification with a fast increase of high-latitude convection when the convection electric field, unshielded by the region 2 current, promptly penetrates to equatorial latitudes as a dawn-dusk electric field. This PPEF usually has eastward polarity on the day sector (Abdu et al., 2013). This eastward electric field enhances the eastward electrojet (EEJ) with the enhanced Cowling conductivity at the dip equator. These eastward PPEFs can intensify the zonal electric field (EF) Ey and the vertical drift **E** x **B**, lifting the ionospheric plasma and enhancing the climatological fountain effect. With these larger electric fields, the dayside equatorial plasma will be lifted to much higher altitudes and latitudes than expected, leading to a positive ionospheric storm (Tsurutani et al., 2008).

Daytime VTEC intensifications were observed for many days during the recovery phase as shown in all case studies. In the Study Cases 1 & 2, the most pronounced daytime intensifications occur on the first day of the recovery phase, just after the $SymH_{min}$. These intensifications could be related to HILDCAA with extended Alfvenic wave trains (Verkhoglyadova et al., 2011, 2013), shallow and fast southward excursions of Bz in the HSS which could lead to intensification in VTEC by the PPEF mechanism, especially at low latitudes. Intensifications higher than 100% were also observed by Candido et al. (2018). They reported VTEC intensifications of over 130% during the CIRs/HSSs interval in 2008, especially at the south crest of the EIA. They attributed these intensifications to both meridional equatorward disturbed winds, which kept the F-region in higher altitudes, and to the continuous and oscillatory nature of Bz, interplanetary electric field (IEF), and AE, which could provide conditions to reinforce equatorial **E** x **B** vertical drifts.

The VTEC depletions, seen as negative ΔVTEC were more pronounced during the daytime, in the recovery phase of the storm, over the equatorial region at around 9 LT (morning) and 15 LT (afternoon), as well as around the crests at 15 LT. These depletions are related to the effects of DDEF. Verkhoglyadova et al. (2013) also proposed that DDEF explains the global thermospheric and ionospheric dynamics during long-duration CIR/HSS intervals by direct energy transfer into the high-latitude ionosphere but takes several hours to a day to take place. This may explain the delay of ∼7 hr for PS, and 18–22 hr for the NS, from the main phases onset time. Worth of noting is that DDEF during the daytime leads to westward electric fields, and consequently the F-region downward movement, when recombination rate is higher.

Finally, percentage positive & negative, δVTEC, were not so significant during daytime for all the regions, as was observed in Tables S8–S10. The most pronounced percentage deviations occurred at nighttime. However, it should be addressed that at nighttime, instrumental and biases calculation limitation can account in the TEC calculation leading to errors (Ma & Maruyama, 2002).

4.2. Nighttime Enhancements/Depletions

The F region electron density of the nighttime ionosphere is expected to decrease steadily during the nighttime when the photoionization induced by solar radiation is absent, and the transport processes are assumed to be ignorable in the classical photoionization theory (L. Liu et al., 2013). However, as seen by other authors (L. Liu et al., 2013; Wang et al., 2022) and in Figures 3–5, this is not what happens during intense and moderate geomagnetic storms. Other studies reported previously that F-layer electron density does not decrease continuously, but sometimes it may increase and lead to significant local peaks, forming nighttime enhancements (Le

et al., 2014; L. Liu et al., 2013; Yadav et al., 2020). Most studies focused on Digisonde measurements and its ionospheric parameters such as fof2, hmF2, and Hm.

Pre-midnight VTEC intensifications in the low-latitude and magnetic equator are related to PREs of the eastward electric field and enhanced upward **E** x **B** drift, which raises the evening equatorial-F region to higher altitudes (Yadav et al., 2020). Post-midnight VTEC intensifications, in turn, are usually caused by equatorward meridional winds pushing the ionization around the EIA crest region toward the equator along the geomagnetic field lines and by westward electric fields (Yadav et al., 2020). In addition to equatorward meridional winds, eastward DDEF leads to upward drifts during nighttime. The DDEF could contribute to nighttime intensifications, especially near sunrise (B. G. Fejer et al., 2008).

Our analysis reveals that intensifications occur principally around pre- and post-midnight. ΔVTEC intensifications, the highest nighttime intensifications are concentrated around the evening and pre-midnight hours. In the dip equator region, maximum intensifications typically occur from 18 LT to 24 LT, with a peak around 21 LT. Most southern crest intensifications occur between 18 LT and 21 LT, especially around 18 LT.

When analyzing δVTEC, the increases occur more frequently at night across all regions. In the equatorial region, most intensifications happen around 21 LT, just before midnight, while in the EIA crests, intensifications are notably higher around 3 LT. According to Immel and Mannucci (2013), during geomagnetic storms, the VTEC enhancements occurring in the American sector are higher than in other sectors. They observed intensifications from 14 LT to 24 LT much higher than in the noon sector. They attributed these intensifications to the redistribution of thermospheric constituents and the downward transport of atomic oxygen near the equator since the production of O^+ may immediately exceed quiet-time levels with the arrival of daylight, particularly from 4 LT to 6 LT, close to the morning terminator.

The nighttime enhancements are in agreement with those observed by Wang et al. (2022), and are classified into three types based on morphology of EIA:

Type 1: A typical EIA structure with two crests around 15°N and 15°S. Unlike the usual behavior, these crests persist throughout the night, gradually closing toward the equator until disappearing around 0 LT.

Type 2: A typical EIA structure either, with crests at 15°N and 15°S, dissipating after sunset with a subsequent increasing in TEC over the equatorial region, as if the plasma is contracting at the magnetic equator. After, this intensification extends to latitudes off-equator, although with weaker intensity.

Type 3: A single prominent crest (northern or southern) until sunset. The TEC then decreases until a surge occurs around 21 LT, initially noticeable in the counter crest. This increase then spreads to the equatorial region and to the other crest, lasting until around 2 LT.

Type 1 Intensifications:

Case 1 (6–7 May 2016): Nighttime enhancements in VTEC were observed at the three regions (crests and equatorial region). These enhancements reached peaks up to 13.5 TECu in the southern crest on 6 May at 19 LT and continued through the night. This continuation of EIA from daytime into nighttime was associated with a weak storm recovery phase ($SymH_{min} > -50$ nT) and supported by Digisonde data indicating elevated h'F and hmF2. The phenomena were linked to eastward undershielding PPEF and auroral heating. These findings are in agreement with J. Liu et al. (2012) and Chingarandi et al. (2023) who observed TEC variations from 15 to 23 TECu in the low latitude ionosphere during a moderate and a minor CIR/HSS-storm, respectively.

Case 2 (1–2 April): VTEC was intensified from daytime through the night across the three regions. However, intensifications on the crests ceased before local midnight. Unfortunately, for this particular case, no Digisonde data were available. The source of these enhancements remains unclear due to the absence of significant geomagnetic disturbances and will be investigate in future work.

Type 2 Intensifications:

Case 1 (7–8 May): During the main phase, new enhancements appeared in the equatorial region and extended to the EIA crests after sunset. Peak VTEC values reached 15 TECu post-midnight at. The h'F and hmF2 showed

increases, but model analyses suggested no significant contributions from PPEF or DDEF on this day. Disturbed meridional winds can be a candidate driver of this enhancements.

Case 3 (11–12 November): A type 2 enhancement occurred after the EIA crests diminished below average daytime values. Intensification was observed in the equatorial region due to westward electric fields.

Type 3 Intensifications:

Case 2 (28–29 March): Initial nighttime enhancement occurred in the southern EIA crest on 28 March 19:48 LT, with ΔVTEC = ∼15 TECu. A similar peak is observed at the northern crest is observed later, on 28 March at 23:53 LT, ΔVTEC = 13 TECu. The enhancement pattern was observed first in the southern crest, followed by the northern crest, indicating a continuation of the EIA during nighttime. The effects of continuous PPEF and DDEF could not be distinctly separated due to the southward Bz component during the recovery phase.

Case 3 (10 November): This enhancement type progressed from the northern crest through the equatorial region to the southern crest, following daytime enhancements. Peak enhancements were 11.4 TECu at boav and 6 TECu at both bele and cuib. The intensification lasted thought the whole night. A decrease of 20 km in h'F indicated this type of enhancement, attributed to the combined effects of PPEF and neutral winds.

Type 1 and Type 2 Combined Intensifications:

Case 3 (7–8 November): During the storm's main phase, enhancements were observed simultaneously at all stations. Peak VTEC values reached 10.8 TECu at the northern crest and 13 TECu in the equatorial region. These enhancements were attributed to the combined effect of upward drift caused by eastward PPEF around dusk and neutral winds. Similar intensifications occurred during the following nights, showing a decrease in h'F followed by a late minor increase, until 6 UT.

5. Summary and Final Considerations

In this work, we present, for the first time, a comprehensive statistical analysis of the influence of moderate and intense geomagnetic storms caused by HSSs, and correlated structures, such as CIRs, on the Brazilian low-latitude ionosphere for the declining phase of SC 24 (years 2016–2017). Our main findings are summarized as follows:

1. From 2016 to 2017 there were 26 geomagnetic storms caused by CIRs/HSSs, of which 23 were moderate and 3 were intense.
2. The storms, on average, lasted 144 hr (6 days), with Vsw_{max}–680 km/s, $SymH_{min}$–70 nT, AE_{max} ∼. In few events, there were sequences of storms associated with sequential coronal holes.
3. The VTEC changes, represented by the ΔVTEC and δVTEC, were highly variable at the equatorial region, around the northern and southern crests of EIA, during the disturbed intervals.
4. The VTEC presented intensifications with respect to the RTEC up to 30 TECu, and significant depletions which were up to 20 TECu.
5. Daytime intensifications occurred during both main and recovery phases of the geomagnetic storm.
6. The intensifications are observed for several days during the recovery of the storms.
7. The case studies presented three types of nighttime enhancement in the equatorial and low-latitude region in Brazil, like the intensifications observed in the Asian-Australian sector by Wang et al., 2022.
8. The delay between the start of the main phase of the storm and the positive variations, in average, was ∼7 hr. And with the negative variations ∼20 hr.

For the first time, catalogs summarizing interplanetary conditions and key VTEC variations during CIR/HSS-driven geomagnetic storms in the descending phase of Solar Cycle 24 have been compiled for the Brazilian longitudinal sector. It's important to note that, while this work focuses on CIRs/HSSs geomagnetic storms, a few ICME-driven storms also occurred but are not detailed in this study. Future research will include ICME-driven storms in the statistics and create detailed maps to better visualize the three types of nighttime enhancements. This work enhances our understanding of the low-latitude ionosphere and space weather during the declining phase of solar activity.

Data Availability Statement

The catalog and images of coronal holes, used to detect High-Speed Streams, can be accessed at Alvestad (2020). Additional coronal hole images were consulted on the archive information hosted by the Gallagher et al. (2020). The CH segmentation/detection was achieved using the methods described in Garton et al. (2018). The OMNI data were obtained from the GSFC/SPDF OMNIWeb interface at https://omniweb.gsfc.nasa.gov. Papitashvili & King, 2020a, 2020b. The RINEX used for GNSS-TEC calculation are provided by Instituto Brasileiro de Geografia e Estatística (2020). The software used calculate the VTEC using the observables is Seemala (2020). Copyright © 2020 Gopi Seemala. All rights reserved. The thermospheric O/N2 data is public available and provided by Paxton (2020). The drifts calculated using magnetometer data were provided by Yizengaw et al. (2020). The drift model is in IRI model (Bilitza, 2018) and the code can be accessed at Fejer and Scherliess (1997b), Fejer and Scherliess (1997a). The five quietest days are sourced by the World Data Center for Geomagnetism, Kyoto.

Acknowledgments

S.P. Moraes-Santos was supported by the Coordination for the Improvement of Higher Education Personnel—Brazil (CAPES)—Financing Code process: 88887.479494/2020-00 and The Abdus Salam International Centre for Theoretical Physics (ICTP) through the Fellowship STEP Programme, which provided opportunities for engagement with experts, participation in workshops, and valuable hospitality. Dr CMN Candido thanks to DAAD/DLR for the funding support in 2022 during her visit to German Aerospace Center DLR, Neustreliz. Dr. V. Klausner was financed in part by the National Council for Scientific and Technological Development (CNPq) under Grant 308258/2021-5. The authors gratefully acknowledge the OMNI data supplied by the GSFC/SPDF OMNIWeb interface at https://omniweb.gsfc.nasa.gov.We would like to express our sincere gratitude to the World Data Center for Geomagnetism, Kyoto, for providing the data on the five quietest days. We are also grateful to the Brazilian Institute of Geography and Statistics (IBGE) for the Brazilian Network for Continuous Monitoring of GNSS Systems (RBMC). Coronal hole information was courtesy of Solen. Info, and the coronal hole image was provided by SolarMonitor.org, hosted by the Dublin Institute for Advanced Studies and SDO/HMI and SDO/AIA consortia. SDO is the first mission launched for NASA's Living with a Star (LWS) Program. We also thank the SAMBA-AMBER network for providing drift daytime data. We gratefully acknowlegde the NASA MO&DA program and Dr. Jarry Paxton for providing the GUVI data. Special thanks to the Aerospace Corporation and the John Hopkins University for designing and building the GUVI instrument. We thank the editor and the reviewers for their time in reviewing the paper. Your expertise and critical feedback have improved the quality of the paper. We want to thank Professor Francisco Javier Azpilicueta for insightful discussions and some help with Fortran. We also extend our gratitude to Professor Bela Fejer and Professor Ludger Scherliess for their assistance with the drift models. We thank the Brazilian Ministry of Science, Technology, and Innovation (MCTI) and the Brazilian Space Agency (AEB).

References

Abalde, J. R., Sahai, Y., Fagundes, P. R., Becker-Guedes, F., Bittencourt, J. A., Pillat, V. G., et al. (2009). Day-to-day variability in the development of plasma bubbles associated with geomagnetic disturbances. *Journal of Geophysical Research*, *114*(4), A04304. https://doi.org/10.1029/2008JA013788

Abdu, M. A. (2001). Outstanding problems in the equatorial ionosphere-thermosphere electrodynamics relevant to spread F. *Journal of Atmospheric and Solar-Terrestrial Physics*, *63*(9), 869–884. https://doi.org/10.1016/S1364-6826(00)00201-7

Abdu, M. A. (2005). Equatorial ionosphere–thermosphere system: Electrodynamics and irregularities. *Advances in Space Research*, *35*(5), 771–787. https://doi.org/10.1016/j.asr.2005.03.150

Abdu, M. A., Medeiros, R. T., Sobral, J. H. A., & Bittencourt, J. A. (1983). Spread F plasma bubble vertical rise velocities determined from spaced ionosonde observations. *Journal of Geophysical Research*, *88*(A11), 9197–9204. https://doi.org/10.1029/JA088iA11p09197

Abdu, M. A., Souza, J. R., Batista, I. S., Fejer, B. G., & Sobral, J. H. A. (2013). Sporadic e layer development and disruption at low latitudes by prompt penetration electric fields during magnetic storms. *Journal of Geophysical Research: Space Physics*, *118*(5), 2639–2647. https://doi.org/10.1002/jgra.50271

Alken, P., Thébault, E., Beggan, C. D., Amit, H., Aubert, J., Baerenzung, J., et al. (2021). International geomagnetic reference field: The thirteenth generation. *Earth Planets and Space*, *73*(1), 49. https://doi.org/10.1186/s40623-020-01288-x

Alves, M. V., Echer, E., & Gonzalez, W. D. (2006). Geoeffectiveness of corotating interaction regions as measured by DST index. *Journal of Geophysical Research*, *111*(7), 1–9. https://doi.org/10.1029/2005JA011379

Alvestad, J. (2020). Coronal hole history [Dataset]. https://solen.info/solar/coronal_holes.html

Anderson, D., Anghel, A., Chau, J., & Veliz, O. (2004). Daytime vertical E × B drift velocities inferred from ground-based magnetometer observations at low latitudes. *Space Weather*, *2*(11), S11001. https://doi.org/10.1029/2004sw000095

Anderson, D., Anghel, A., Yumoto, K., Ishitsuka, M., & Kudeki, E. (2002). Estimating daytime vertical ExB drift velocities in the equatorial F-region using ground-based magnetometer observations. *Geophysical Research Letters*, *29*(12), 4–7. https://doi.org/10.1029/2001GL014562

Azzouzi, I., Migoya-Orue, Y. O., Coisson, P., Amory-Mazaudier, C., Fleury, R., & Radicella, S. M. (2016). Day-to-day variability of VTEC and ROTI in October 2012 with impact of high-speed solar wind stream on 13 October 2012. *Sun and Geosphere*, *11*, 7–22.

Balan, N., & Rao, P. B. (1990). Dependence of ionospheric response on the local time of sudden commencement and the intensity of geomagnetic storms. *Journal of Atmospheric and Terrestrial Physics*, *52*(4), 269–275. https://doi.org/10.1016/0021-9169(90)90094-4

Balan, N., Yamamoto, M., Liu, J. Y., Otsuka, Y., Liu, H., & Lühr, H. (2011). New aspects of thermospheric and ionospheric storms revealed by CHAMP. *Journal of Geophysical Research*, *116*(7), A07305. https://doi.org/10.1029/2010JA016399

Batista, I. S., de Souza, J. R., Abdu, M. A., & de Paula, E. R. (1994). Total electron content at low latitudes and its comparison with the IRI90. *Advances in Space Research*, *14*(12), 87–90. https://doi.org/10.1016/0273-1177(94)90246-1

Bilitza, D. (2018). IRI the international standard for the ionosphere. *Advances in Radio Science*, *16*, 1–11. https://doi.org/10.5194/ars-16-1-2018

Bilitza, D., Pezzopane, M., Truhlik, V., Altadill, D., Reinisch, B. W., & Pignalberi, A. (2022). The international reference ionosphere model: A review and description of an ionospheric benchmark. In *Reviews of geophysics*, (Vol. 60(4)) John Wiley and Sons Inc. https://doi.org/10.1029/2022RG000792

Blanc, M., & Richmond, A. D. (1980). The ionospheric disturbance dynamo. *Journal of Geophysical Research*, *85*(9), 1669–1686. https://doi.org/10.1029/ja085ia04p01669

Borovsky, J. E., & Steinberg, J. T. (2006). The "calm before the storm" in CIR/magnetosphere interactions: Occurrence statistics, solar wind statistics, and magnetospheric preconditioning. *Journal of Geophysical Research*, *111*(7), 1–29. https://doi.org/10.1029/2005JA011397

Burke, W. J., Huang, C. Y., Gentile, L. C., & Bauer, L. (2004). Seasonal-longitudinal variability of equatorial plasma bubbles. *Annales Geophysicae*, *22*(9), 3089–3098. https://doi.org/10.5194/angeo-22-3089-2004

Candido, C. M. N., Batista, I. S., Klausner, V., de Siqueira Negreti, P. M., Becker-Guedes, F., de Paula, E. R., et al. (2018). Response of the total electron content at Brazilian low latitudes to corotating interaction region and high-speed streams during solar minimum 2008. *Earth Planets and Space*, *70*(1), 104. https://doi.org/10.1186/s40623-018-0875-8

Chakraborty, M., Kumar, S., Kumar De, B., & Guha, A. (2015). Effects of geomagnetic storm on low latitude ionospheric total electron content: A case study from Indian sector. *Journal of Earth System Science*, *124*(5), 1115–1126. https://doi.org/10.1007/s12040-015-0588-3

Chakraborty, S., Ray, S., Sur, D., Datta, A., & Paul, A. (2020). Effects of CME and CIR induced geomagnetic storms on low-latitude ionization over Indian longitudes in terms of neutral dynamics. *Advances in Space Research*, *65*(1), 198–213. https://doi.org/10.1016/j.asr.2019.09.047

Chingarandi, F. S., Candido, C. M. N., Becker-Guedes, F., Jonah, O. F., Moraes-Santos, S. P., Klausner, V. I., & Taiwo, O. O. (2023). Assessing the effects of a minor CIR-HSS geomagnetic storm on the Brazilian low-latitude ionosphere: Ground and space-based observations. *Space Weather*, *21*(9), e2023SW003500. https://doi.org/10.1029/2023sw003500

Emery, B. A., Richardson, I. G., Evans, D. S., Rich, F. J., & Wilson, G. R. (2011). Solar rotational periodicities and the semiannual variation in the solar wind, radiation Belt, and Aurora. *Solar Physics*, *274*(1–2), 399–425. https://doi.org/10.1007/s11207-011-9758-x

Farid, H. M., Mawad, R., Ghamry, E., & Yoshikawa, A. (2020). The impact of coronal mass ejections on the seasonal variation of the ionospheric critical frequency f0F2. *Universe*, *6*(11), 200. https://doi.org/10.3390/universe6110200

Fejer, B., & Scherliess, L. (1997a). Empirical vertical drifts model for storm time [Code]. *International Reference Ionosphere*. https://irimodel.org/IRI-2020/

Fejer, B. G. (2011). Low latitude ionospheric electrodynamics. *Space Science Reviews*, *158*(1), 145–166. https://doi.org/10.1007/s11214-010-9690-7

Fejer, B. G., Blanc, M., & Richmond, A. D. (2017). Post-storm middle and low-latitude ionospheric electric fields effects. In *Space science reviews*, (Vol. 206(1–4), pp. 407–429). Springer. https://doi.org/10.1007/s11214-016-0320-x

Fejer, B. G., Gonzales, C. A., Farley, D. T., Kelley, M. C., & Woodman, R. F. (1979). Equatorial electric fields during magnetically disturbed conditions—1. The effect of the interplanetary magnetic field. *Journal of Geophysical Research*, *84*(A10), 5797–5802. https://doi.org/10.1029/JA084iA10p05797

Fejer, B. G., Jensen, J. W., & Su, S. Y. (2008). Seasonal and longitudinal dependence of equatorial disturbance vertical plasma drifts. *Geophysical Research Letters*, *35*(20), 2–5. https://doi.org/10.1029/2008GL035584

Fejer, B. G., & Scherliess, L. (1997b). Empirical models of storm time equatorial zonal electric fields. *Journal of Geophysical Research*, *102*(A11), 24047–24056. https://doi.org/10.1029/97JA02164

Gallagher, P. T., Carley, E., & McCloskey, A. (2020). Solar Monitor's coronal hole segmentations are performed by CHIMERA [Dataset]. https://www.solarmonitor.org/chimera.php?date=20200515

Garton, T. M., Gallagher, P. T., & Murray, S. A. (2018). Automated coronal hole identification via multi-thermal intensity segmentation. *Journal of Space Weather and Space Climate*, *8*(2005), A02. https://doi.org/10.1051/swsc/2017039

Gibson, S. E., Kozyra, J. U., De Toma, G., Emery, B. A., Onsager, T., & Thompson, B. J. (2009). If the sun is so quiet, why is the earth ringing? A comparison of two solar minimum intervals. *Journal of Geophysical Research*, *114*(9), 1–7. https://doi.org/10.1029/2009JA014342

Gonzalez, W. D., Joselyn, J. A., Kamide, Y., Kroehl, H. W., Rostoker, G., Tsurutani, B. T., & Vasyliunas, V. M. (1994). What is a geomagnetic storm? *Journal of Geophysical Research*, *99*(A4), 5771–5792. https://doi.org/10.1029/93ja02867

Grandin, M., Aikio, A. T., Kozlovsky, A., Ulich, T., & Raita, T. (2015). Effects of solar wind high-speed streams on the high-latitude ionosphere: Superposed epoch study. *Journal of Geophysical Research: Space Physics*, *120*(12), 10669–10687. https://doi.org/10.1002/2015JA021785

Hanson, E., Okeke, F. N., & Okpala, K. (2019). Investigation of effects of coronal mass ejections on ionospheric total electron content over Nsukka, South Eastern Nigeria. *Investigation of Effects of Coronal Mass Ejections on Ionospheric Total Electron Content over Nsukka, South Eastern Nigeria, April*, 1–10. https://doi.org/10.5194/angeo-2019-39

Immel, T. J., & Mannucci, A. J. (2013). Ionospheric redistribution during geomagnetic storms. *Journal of Geophysical Research: Space Physics*, *118*(12), 7928–7939. https://doi.org/10.1002/2013JA018919

Instituto Brasileiro de Geografia e Estatística. (2020). Brazilian network for continuous monitoring of GNSS systems [Dataset]. https://www.ibge.gov.br/en/geosciences/geodetic-positioning/geodetic-networks/20079-brazilian-network-for-continuous-monitoring-gnss-systems.html?lang=en-GB

Kavanagh, A., & Denton, M. (2007). Wind streams and geospace interactions. *Astronomy and Geophysics*, *48*(6), 6.24–6.26.

Kelley, M. C., & Dao, E. (2009). On the local time dependence of the penetration of solar wind-induced electric fields to the magnetic equator. *Annales Geophysicae*, *27*(8), 3027–3030. https://doi.org/10.5194/angeo-27-3027-2009

Kivelson, M. G., Russell, C. T., & Brown, M. E. (1996). Introduction to space Physics. Physics today. *Physics Today*, *49*(4), 57–58. https://doi.org/10.1063/1.2807586

Koga, D., Sobral, J. H. A., Gonzalez, W. D., Arruda, D. C. S., Abdu, M. A., de Castilho, V. M., et al. (2011). Electrodynamic coupling processes between the magnetosphere and the equatorial ionosphere during a 5-day HILDCAA event. *Journal of Atmospheric and Solar-Terrestrial Physics*, *73*(1), 148–155. https://doi.org/10.1016/j.jastp.2010.09.002

Kutiev, I., Otsuka, Y., Pancheva, D., & Heelis, R. (2012). Response of low-latitude ionosphere to medium-term changes of solar and geomagnetic activity. *Journal of Geophysical Research*, *117*(A8), A08330. https://doi.org/10.1029/2012JA017641

Laundal, K. M., & Richmond, A. D. (2017). Magnetic coordinate systems. In *Space science reviews*, (Vol. 206(1–4), pp. 27–59). Springer. https://doi.org/10.1007/s11214-016-0275-y

Le, H., Liu, L., Chen, Y., Zhang, H., & Wan, W. (2014). Modeling study of nighttime enhancements in F region electron density at low latitudes. *Journal of Geophysical Research: Space Physics*, *119*(8), 6648–6656. https://doi.org/10.1002/2013ja019295

Lei, J., Thayer, J. P., Forbes, J. M., Wu, Q., She, C., Wan, W., & Wang, W. (2008). Ionosphere response to solar wind high-speed streams. *Geophysical Research Letters*, *35*(19), 1–5. https://doi.org/10.1029/2008GL035208

Liu, H., Yamazaki, Y., & Lei, J. (2021). Day-to-Day variability of the thermosphere and ionosphere. *Space Physics and Aeronomy, Upper Atmosphere Dynamics and Energetics*, *4*, 275–300. https://doi.org/10.1002/9781119815631.ch15

Liu, J., Liu, L., Zhao, B., Wei, Y., Hu, L., & Xiong, B. (2012). High-speed stream impacts on the equatorial ionization anomaly region during the deep solar minimum year 2008. *Journal of Geophysical Research*, *117*(10), 1–12. https://doi.org/10.1029/2012JA018015

Liu, J., Zhao, B., & Liu, L. (2010a). Time delay and duration of ionospheric total electron content responses to geomagnetic disturbances. *Annales Geophysicae*, *28*(3), 795–805. https://doi.org/10.5194/angeo-28-795-2010

Liu, L., Chen, Y., Le, H., Ning, B., Wan, W., Liu, J., & Hu, L. (2013). A case study of postmidnight enhancement in F-layer electron density over Sanya of China. *Journal of Geophysical Research: Space Physics*, *118*(7), 4640–4648. https://doi.org/10.1002/jgra.50422

Liu, L., He, M., Yue, X., Ning, B., & Wan, W. (2010b). Ionosphere around equinoxes during low solar activity. *Journal of Geophysical Research*, *115*(9), 1–10. https://doi.org/10.1029/2010JA015318

Loewe, C. A., & Prölss, G. W. (1997). Classification and mean behavior of magnetic storms. *Journal of Geophysical Research A: Space Physics*, *102*(A7), 14209–14213. https://doi.org/10.1029/96JA04020

Ma, G., & Maruyama, T. (2002). Derivation of TEC and estimation of instrumental biases from GEONET in Japan. *Journal of the Communications Research Laboratory*, *49*(4), 121–133.

Mannucci, A. J., Tsurutani, B. T., Iijima, B. A., Komjathy, A., Saito, A., Gonzalez, W. D., et al. (2005). Dayside global ionospheric response to the major interplanetary events of October 29–30, 2003 "Halloween Storms.". *Geophysical Research Letters*, *32*(12), 1–4. https://doi.org/10.1029/2004GL021467

Matamba, T. M., & Habarulema, J. B. (2018). Ionospheric responses to CME- and CIR-driven geomagnetic storms along 30°E–40°E over the African sector from 2001 to 2015. *Space Weather*, *16*(5), 538–556. https://doi.org/10.1029/2017SW001754

McClure, J. P., Hanson, W. B., & Hoffman, J. H. (1977). Plasma bubbles and irregularities in the equatorial ionosphere. *Journal of Geophysical Research*, *82*(19), 2650–2656. https://doi.org/10.1029/ja082i019p02650

Migoya-Orue, Y. O., Azzouzi, I., Coisson, P., Amory-mazaudier, C., Fleury, R., & Radicella, S. M. (2016). Ionospheric and magnetic signatures of a high speed solar wind in low latitudes on 13 October. *Sun and Geosphre*, *11*(1), 101–113.

Mishra, R. K., Adhikari, B., Chapagain, N. P., Baral, R., Das, P. K., Klausner, V., & Sharma, M. (2020). Variation on solar wind parameters and total electron content over middle-to low-latitude regions during intense geomagnetic storms. *Radio Science*, *55*(11), e2020RS007129. https://doi.org/10.1029/2020RS007129

Nakagawa, Y., Nozawa, S., & Shinbori, A. (2019). Relationship between the low-latitude coronal hole area, solar wind velocity, and geomagnetic activity during solar cycles 23 and 24. *Earth Planets and Space*, *71*(1), 15. https://doi.org/10.1186/s40623-019-1005-y

Natras, R., Soja, B., & Schmidt, M. (2022). Ensemble machine learning of random forest, AdaBoost and XGBoost for forecasting vertical total electron content of the ionosphere ensemble machine learning of random forest, AdaBoost and XGBoost for forecasting vertical total electron content of the io. *Journal of Geodesy*, 1–34.

Navarro, L. A., Fejer, B. G., & Scherliess, L. (2019). Equatorial disturbance dynamo vertical plasma drifts over Jicamarca: Bimonthly and solar cycle dependence. *Journal of Geophysical Research: Space Physics*, *124*(6), 4833–4841. https://doi.org/10.1029/2019JA026729

Negreti, P. M. S., de Paula, E. R., & Candido, C. M. N. (2017). Total electron content responses to HILDCAAs and geomagnetic storms over South America. *Annales Geophysicae*, *35*(6), 1309–1326. https://doi.org/10.5194/angeo-35-1309-2017

Ogwala, A., Somoye, E. O., Ogunmodimu, O., Adeniji-Adele, R. A., Onori, E. O., & Oyedokun, O. (2019). Diurnal, seasonal and solar cycle variation in total electron content and comparison with IRI-2016 model at Birnin Kebbi. *Annales Geophysicae*, *37*(5), 775–789. https://doi.org/10.5194/angeo-37-775-2019

Otsuka, Y., Suzuki, K., Nakagawa, S., Nishioka, M., Shiokawa, K., & Tsugawa, T. (2013). GPS observations of medium-scale traveling ionospheric disturbances over Europe. *Annales Geophysicae*, *31*(2), 163–172. https://doi.org/10.5194/angeo-31-163-2013

Papitashvili, N. E., & King, J. H. (2020a). OMNI 1-min data [Dataset]. *NASA Space Physics Data Facility*. https://doi.org/10.48322/45bb-8792

Papitashvili, N. E., & King, J. H. (2020b). OMNI hourly data [Dataset]. *NASA Space Physics Data Facility*. https://doi.org/10.48322/1shr-ht18

Paxton, L. J. (2020). Thermospheric O/N2 gallery [Dataset]. *The Aerospace Corporation and The Johns Hopkins University*. https://guvitimed.jhuapl.edu/index.php/guvi-galleryl3on2

Pedatella, N. M., & Forbes, J. M. (2011). Electrodynamic response of the ionosphere to high-speed solar wind streams. *Journal of Geophysical Research*, *116*(12), 1–12. https://doi.org/10.1029/2011JA017050

Pereira Silva, R., Humberto Andrade Sobral, J., Koga, D., & Rodrigues Souza, J. (2017). Evidence of prompt penetration electric fields during HILDCAA events. *Annales Geophysicae*, *35*(5), 1165–1176. https://doi.org/10.5194/angeo-35-1165-2017

Pereira Silva, R., Marcos Denardini, C., Soares Marques, M., Cristina Araujo Resende, L., Moro, J., Arlan Da Silva Picanço, G., et al. (2020). Ionospheric total electron content responses to HILDCAA intervals. *Annales Geophysicae*, *38*(1), 27–34. https://doi.org/10.5194/angeo-38-27-2020

Rastogi, R. G. (1980). Seasonal variation of equatorial spread F in the American. *Journal of Geophysical Research*, *85*(9), 722–726. https://doi.org/10.1029/ja085ia02p00722

Richardson, I. G. (2013). The Formation of CIRs at stream-stream interfaces and resultant geomagnetic activity. *Recurrent Magnetic Storms: Corotating Solar Wind Streams*, 45–58. https://doi.org/10.1029/167GM06

Richardson, I. G. (2018). Solar wind stream interaction regions throughout the heliosphere. *Living Reviews in Solar Physics*, *15*(1), 1. https://doi.org/10.1007/s41116-017-0011-z

Richardson, I. G., & Cane, H. V. (2010). Near-earth interplanetary coronal mass ejections during solar cycle 23 (1996–2009): Catalog and summary of properties. *Solar Physics*, *264*(1), 189–237. https://doi.org/10.1007/s11207-010-9568-6

Richardson, I. G., Webb, D. F., Zhang, J., Berdichevsky, D. B., Biesecker, D. A., Kasper, J. C., et al. (2006). Major geomagnetic storms (Dst ≤ -100 nT) generated by corotating interaction regions. *Journal of Geophysical Research*, *111*(7), 1–17. https://doi.org/10.1029/2005JA011476

Richmond, A. D., Peymirat, C., & Roble, R. G. (2003). Long-lasting disturbances in the equatorial ionospheric electric field simulated with a coupled magnetosphere-ionosphere-thermosphere model. *Journal of Geophysical Research*, *108*(A3), 1–12. https://doi.org/10.1029/2002JA009758

Santos, A. M., Abdu, M. A., Souza, J. R., Sobral, J. H. A., Batista, I. S., & Denardini, C. M. (2016). Storm time equatorial plasma bubble zonal drift reversal due to disturbance Hall electric field over the Brazilian region. *Journal of Geophysical Research: Space Physics*, *111*(7), 5594–5612. https://doi.org/10.1029/2006JA011892

Scherliess, L., & Fejer, B. G. (1999). Radar and satellite global equatorial F region vertical drift model. *Journal of Geophysical Research*, *104*(A4), 6829–6842. https://doi.org/10.1029/1999ja900025

Seemala, G. K. (2012). GPS-TEC analysis application (Issue May).

Seemala, G. K. (2020). GPS-TEC analysis application [Software]. https://seemala.blogspot.com/

Seemala, G. K., & Valladares, C. E. (2011). Statistics of total electron content depletions observed over the South American continent for the year 2008. *Radio Science*, *46*(5), 1–14. https://doi.org/10.1029/2011RS004722

Tapping, K. F. (2013). The 10.7 cm solar radio flux (F10.7). *Space Weather*, *11*(7), 394–406. https://doi.org/10.1002/swe.20064

Tsurutani, B. T., Gonzalez, W. D., Gonzalez, A. L. C., Guarnieri, F. L., Gopalswamy, N., Grande, M., et al. (2006). Corotating solar wind streams and recurrent geomagnetic activity: A review. *Journal of Geophysical Research*, *111*(A7), 1–25. https://doi.org/10.1029/2005JA011273

Tsurutani, B. T., Verkhoglyadova, O. P., Mannucci, A. J., Saito, A., Araki, T., Yumoto, K., et al. (2008). Prompt Penetration Electric Fields (PPEFs) and their ionospheric effects during the great magnetic storm of 30–31 October 2003. *Journal of Geophysical Research*, *113*(5), 1–10. https://doi.org/10.1029/2007JA012879

Tulasi Ram, S., Kumar, S., Su, S. Y., Veenadhari, B., & Ravindran, S. (2015). The influence of Corotating Interaction Region (CIR) driven geomagnetic storms on the development of Equatorial Plasma Bubbles (EPBs) over wide range of longitudes. *Advances in Space Research*, *55*(2), 535–544. https://doi.org/10.1016/j.asr.2014.10.013

Valladares, C. E., Villalobos, J., Hei, M. A., Sheehan, R., Basu, S., MacKenzie, E., et al. (2009). Simultaneous observation of traveling ionospheric disturbances in the Northern and Southern Hemispheres. *Annales Geophysicae*, *27*(4), 1501–1508. https://doi.org/10.5194/angeo-27-1501-2009

Venkatesh, K., Fagundes, P. R., Prasad, D. S. V. V. D., Denardini, C. M., Abreu, A. J., Jesus, R., et al. (2015). Day-to-day variability of equatorial electrojet and its role on the day-to-day characteristics of the equatorial ionization anomaly over the Indian and Brazilian sectors. *Journal of Geophysical Research A: Space Physics*, *120*(10), 9117–9131. https://doi.org/10.1002/2015JA021307

Verkhoglyadova, O. P., Tsurutani, B. T., Mannucci, A. J., Mlynczak, M. G., Hunt, L. A., Komjathy, A., & Runge, T. (2011). Ionospheric VTEC and thermospheric infrared emission dynamics during corotating interaction region and high-speed stream intervals at solar minimum: 25 March to 26 April 2008. *Journal of Geophysical Research*, *116*(9). https://doi.org/10.1029/2011JA016604

Verkhoglyadova, O. P., Tsurutani, B. T., Mannucci, A. J., Mlynczak, M. G., Hunt, L. A., & Runge, T. (2013). Variability of ionospheric TEC during solar and geomagnetic minima (2008 and 2009): External high speed stream drivers. *Annales Geophysicae*, *31*(2), 263–276. https://doi.org/10.5194/angeo-31-263-2013

Wang, Y., Huang, F., Lei, J., Luan, X., Dou, X., & Owolabi, C. (2022). Ionospheric nighttime enhancements in the equatorial region as revealed by the Beidou geostationary TEC observations. *Journal of Geophysical Research: Space Physics*, *127*(8). https://doi.org/10.1029/2022JA030483

Yadav, S., Choudhary, R. K., Kumari, J., Sunda, S., Shreedevi, P. R., & Pant, T. K. (2020). Reverse fountain and the nighttime enhancement in the ionospheric electron density over the equatorial region: A case study. *Journal of Geophysical Research: Space Physics*, *125*(5). https://doi.org/10.1029/2019JA027286

Yeeram, T. (2017). Interplanetary drivers of daytime penetration electric field into equatorial ionosphere during CIR-induced geomagnetic storms. *Journal of Atmospheric and Solar-Terrestrial Physics*, *157–158*, 6–15. https://doi.org/10.1016/j.jastp.2017.02.008

Yizengaw, E., & Moldwin, M. B. (2009). African meridian b-field education and research (Amber) array. *Earth, Moon, and Planets*, *104*(1–4), 237–246. https://doi.org/10.1007/s11038-008-9287-2

Yizengaw, E., Zesta, E., Moldwin, M., & Boudouridis, A. (2020). E x B Drift from SAMBA-AMBER [Dataset]. *SAMBA-AMBER*. https://magnetometers.bc.edu/data/electrojets/

Zhang, Y., Wu, Z., Feng, J., Xu, T., Deng, Z., Ou, M., & Xiong, W. (2021). Time delay of ionospheric TEC storms to geomagnetic storms and pre-storm disturbance events in East Asia. *Advances in Space Research*, *67*(5), 1535–1545. https://doi.org/10.1016/j.asr.2020.11.026

Zhou, W., Song, S., Chen, Q., Cheng, N., & Xie, H. (2018). Determination of nighttime VTEC average in the Klobuchar ionospheric delay model. *Geodesy and Geodynamics*, *9*(2), 175–182. https://doi.org/10.1016/j.geog.2017.09.001